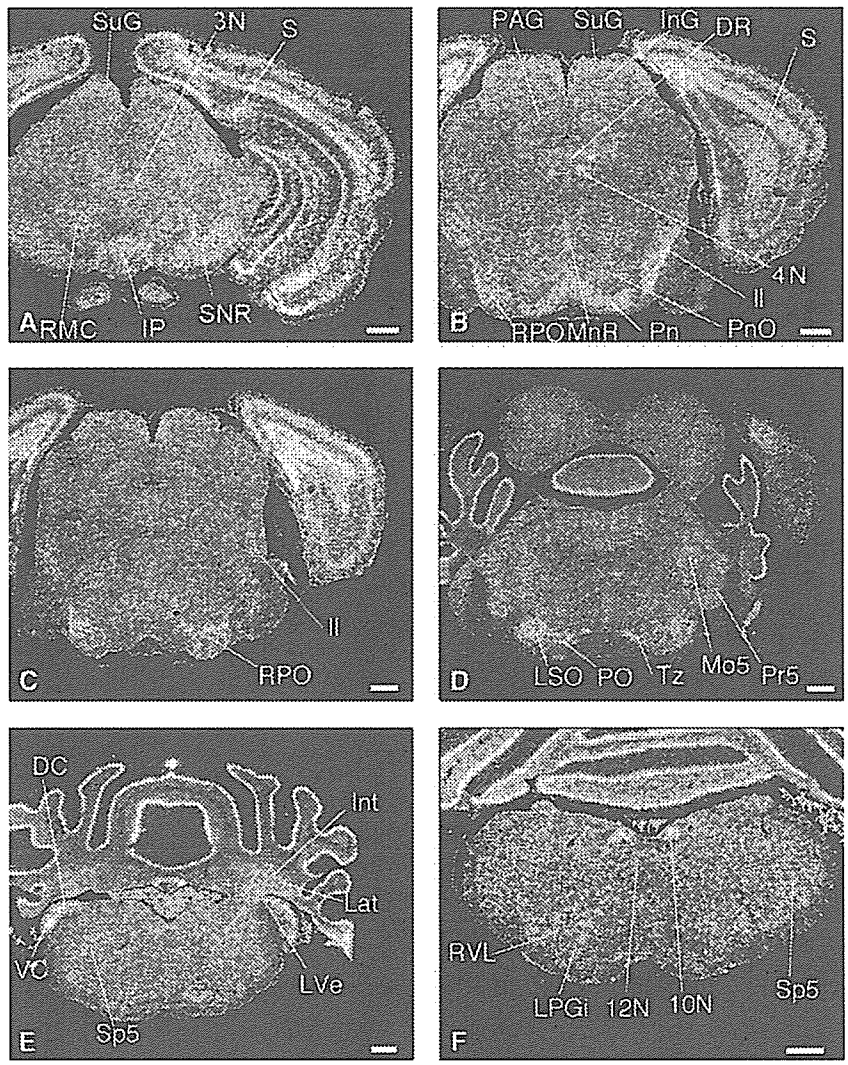

Fig. 2 – Expression of Id2 mRNA in the brainstem. Dark field photomicrographs showing Id2 mRNA expression in coronal sections. Strong expression was observed in the pontine nuclei, lateral lemniscus (B), dorsal and ventral cochlear nucleus (E), and dorsal motor nucleus of vagus (F). Scale bar, 500 m. Abbreviations are listed in Table 1.

1991). We examined the regional expression level of Id2 in the adult mouse brain. Total RNA was purified from the cerebral cortex, cerebellum, and caudate putamen of the adult mouse brain. Twenty micrograms of total RNA was separated by electrophoresis on a 1.0% agarose-formaldehyde gel, transferred onto filters, and cross-linked in a UV chamber. Hybridization with the probe derived from the full-length Id2 cDNA and washing were performed under high stringency conditions as described (Mori et al., 2000). X-ray films were exposed with an intensifying screen at −80 °C for 72 h. As shown in Fig. 3G, Id2 expression was high in the cerebral cortex and cerebellum and low in the caudate putamen.

The Id gene family consists of 4 members, Id1–Id4. To examine the difference of their expression patterns in the adult mouse brain, we performed in situ hybridization with the respective radiolabeled probes. The probes for Id1, Id3, and Id4 corresponded to the regions spanning nt 1–927, nt 560–969, and nt 2927–4701 of the respective cDNAs (Benezra et al., 1990; Christy et al., 1991; Riechmann et al., 1994). Since no apparent signal was detected for Id1 mRNA, we show the results for the expression of Id3 and Id4 mRNAs. Although Id3 mRNA was detected in many brain regions at a low or moderate level, some specific regions showed higher expression. In the main olfactory bulb, Id3 mRNA was expressed in the glomerular layer (Gl) (Fig. 4A). In the septum, Id3 mRNA was expressed in the medial septal nucleus (MS) and triangular septal nucleus (TS) (Figs. 4B and C). In the stria medullaris of the thalamus (sm), stria terminalis (st), habenular commissure (hbc), and medial habenular nucleus (MHb), Id3 mRNA was moderately expressed (Figs. 4C and D). Some Id3-expressing cells were also distributed in the corpus callosum (cc), external and internal capsule (ec, ic), and cingulum (cg) (Figs. 4B, D, and E). In the cerebral cortex, Id3 mRNA was detected in layers 5 and 6, and scattered cells were positive for Id3 mRNA in layer 1 (Figs. 4B–E). Some cells were moderately labeled in the caudate putamen (CPu) and lateral globus pallidus (LGP) (Figs. 4B and C). In the SVZ–ependymal region, some cells were labeled (Fig. 8B). In the hippocampus, Id3 was expressed in the molecular layer of the dentate gyrus (Mol) (Figs. 4D and E). Moderately labeled cells were scattered in the posterior thalamic nuclear

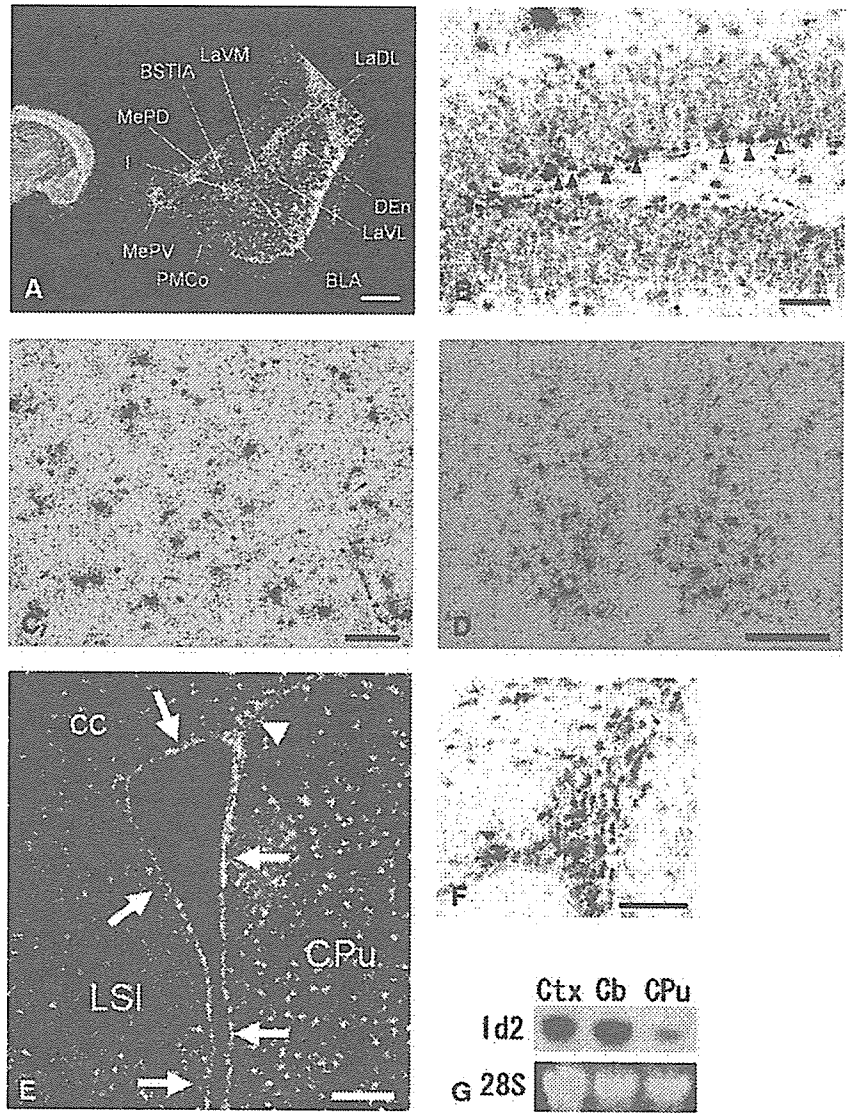

Fig. 3 – Expression of Id2 mRNA in the brain regions. (A) Dark field photomicrographs showing Id2 mRNA expression in the amygdala. Coronal sections. High magnification of the area indicated by a square is shown on the right. Id2 mRNA expression was observed widely in the subnuclei in the amygdala. Strong expression was observed in the dorsal endopiriform nucleus, lateral amygdaloid nucleus dorsolateral part and ventromedial part, medial amygdaloid nucleus posterodorsal part and posteroventral part, intercalated nuclei. Scale bar, 500 m. Abbreviations are listed in Table 1. (B) Bright field photomicrograph showing high magnification of the granule layer and subgranular zone of the hippocampus. Note that Id2 mRNA was detected in the subgranular zone of the dentate where neurogenesis is known to occur (arrowheads). Most of the granule cells and pyramidal cells were not labeled. Scale bar, 50 m. (C) Bright field photomicrograph showing Id2 mRNA expression in the caudate putamen. Strongly labeled cells were scattered sparsely in the caudate putamen. Scale bar, 100 m. (D) Bright field photomicrograph showing Id2 mRNA expression in the suprachiasmatic nucleus. Scale bar, 200 m. (E) Dark field photomicrograph showing the expression of Id2 mRNA in the subventricular zone–ependymal region (arrow) and anterior part of the subventricular zone (SVZa) (arrowhead). Scale bar, 200 m. Abbreviations are listed in Table 1. (F) Bright field photomicrograph showing higher magnification of SVZa. Scale bar, 100 m. (G) Northern blot analysis for Id2 expression. Total RNA was isolated from the cerebral cortex (Ctx), cerebellum (Cb), and caudate putamen (CPu) of the adult mouse brain and subjected to Northern blotting. Twenty-eight S ribosomal RNA is shown as a loading control.

group (Po), ventral posteromedial thalamic nucleus (VPM), and ventral posterolateral thalamic nucleus (VPL) (Fig. 4D). In the midbrain, Id3 was expressed in the interpeduncular nucleus, rostral subnucleus (IPR) (Fig. 4E). On the other hand, the expression level of Id4 mRNA was low, and long exposure was required to obtain signals. Although we encountered high background, some regions were identified as positive for Id4 expression. In the main olfactory bulb, Id4 mRNA was expressed in the anterior commissure, intrabulbar part (aci), and glomerular layer (Gl) (Fig. 5A). In the caudate putamen, some cells were labeled (Fig. 5B). In the SVZ–ependymal region, some cells were labeled (Fig. 5B). Id4 mRNA expression

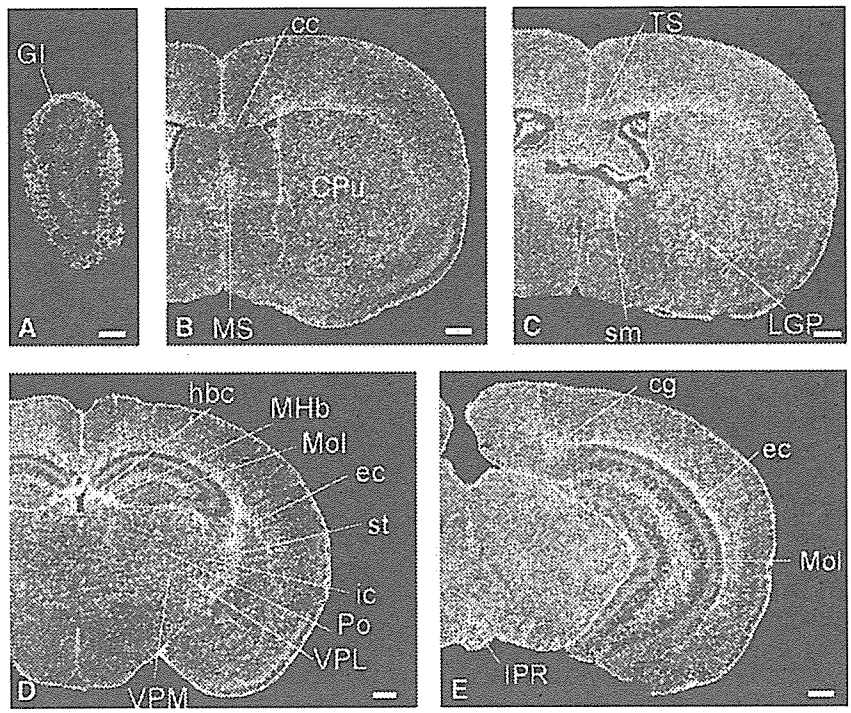

Fig. 4 – Id3 mRNA expression in the brain. Dark field photomicrographs showing Id3 mRNA expression in coronal sections. Strong expression was observed in the medial septal nucleus (B), stria medullaris of the thalamus (C), molecular layer of the dentate gyrus, external capsule, internal capsule (D), and cingulum (E). Scale bar, 500 m. Abbreviations are listed in Table 1.

was observed in the lateral amygdaloid nucleus dorsolateral part (LaDL), ventromedial part (LaVM), and medial amygdaloid nucleus posterodorsal part (MePD) (Fig. 5C). In the brainstem, Id4 mRNA was expressed in the interpeduncular nucleus, lateral and rostral subnuclei (IPL, IPR), and dorsal raphe nucleus, dorsal and ventral parts (DRD, DRV) (Fig. 5E). These

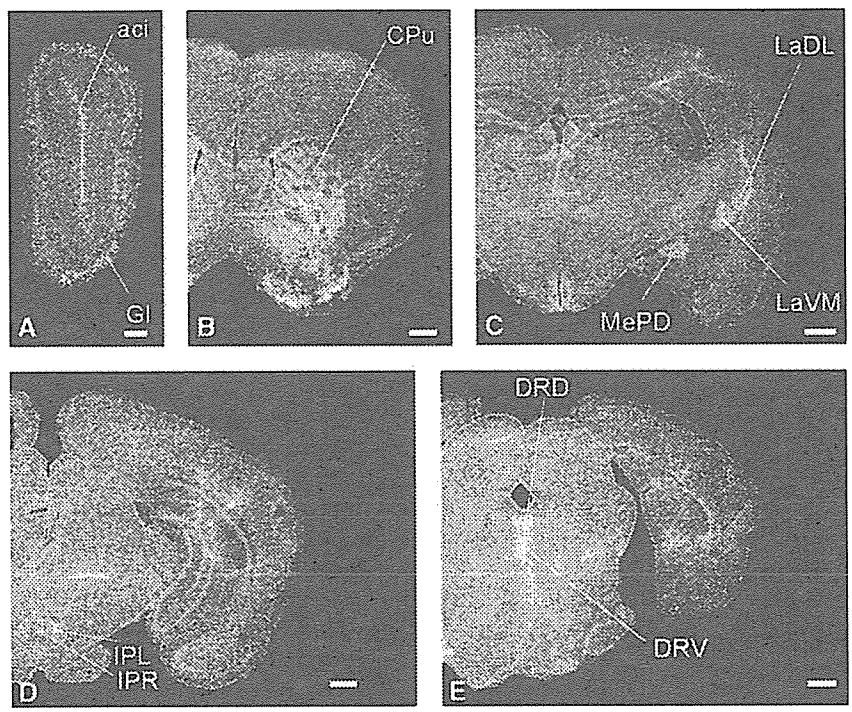

Fig. 5 – Expression of Id4 mRNA in the brain. Dark field photomicrographs showing Id4 mRNA expression in coronal sections. Expression was observed in the caudate putamen (B), lateral amygdaloid nucleus, dorsolateral and ventromedial part, medial amygdaloid nucleus, posterodorsal part (C), interpeduncular nucleus, lateral and rostral subnucleus (D), and dorsal raphe nucleus, dorsal and ventral parts (E). Scale bar, 500 m. Abbreviations are listed in Table 1.

Table 2 – Summary of Id2 and Id3 expression in the adult mouse brain

	Id2	Id3
Forebrain		
Main olfactory bulb		
Mitral cell layer	++	+
Glomerular layer	++	++
Granule cell layer	+	+
Anterior olfactory nucleus	+	+
Septum		
Lateral septal nucleus	+	+
Medial septal nucleus	–	++
Triangular septal nucleus	–	++
Corpus callosum	+[a]	++
Stria terminalis	–	++
External capsule	–	++
Internal capsule	–	++
Habenular commissure	–	++
Medial habenular nucleus	–	++
Cingulum	–	++
Cerebral cortex		
Neo cortex		
Layer 1	+[a]	+
Layer 2	++	+
Layer 3	++	+
Layer 4	–	+
Layer 5	+++	++
Layer 6	++	++
Amygdaloid complex		
Basolateral, anterior part	+++	+
Lateral		
Dorsolateral part	+++	+
Ventromedial part	+++	+
Ventrolateral part	+++	+
Medial		
Posterodorsal part	+++	+
Posteroventral part	+++	+
Anterior cortical	+++	+
Posteromedial cortical	+++	+
Intercalated nuclei	+++	+
Other subnuclei	++	+
Anterior amygdaloid area	++	+
Hippocampus		
Subgranular zone	++[a]	+
Subiculum	+++	+
Molecular layer	+[a]	+++
Nucleus of the lateral olfactory tract	++	+
Dorsal endopiriform nucleus	+++	+
Bed nucleus of stria terminalis	++	+
Intraamygdaloid division of the bed nucleus of the stria terminalis	++	+
Globus pallidus	++	++
Caudate putamen	+[a]	++[a]
Subventricular zone–ependymal region	++	++
Anterior part of the subventricular zone	+++	+
Ventral pallidum	++	+
Thalamus		
Ventral anterior nucleus	++	+
Ventral posteromedial nucleus	++	++[a]
Ventral posterolateral nucleus	–	++[a]
Posterior thalamic nuclear group	–	++[a]
Geniculate nucleus	++	+
Other subnuclei	+	+
Subthalamic nucleus	++	+
Hypothalamus		
Paraventricular hypothalamic nucleus anterior parvicellular part	++	+
Dorsomedial hypothalamic nucleus	++	+
Other nuclei	+	+
Suprachiasmatic nuclei	++	+
Midbrain		
Substantia nigra		
Pars compacta	–	+
Pars reticulata	++	+
Pars lateralis	–	+
Ventral tegmental area	–	+
Interpeduncular nucleus	++	++
Medial terminal nucleus of the accessory optic tract	+++	+
Red nucleus	++	+
Superior colliculus	++	+
Oculomotor nucleus	+	+
Trochlear nucleus	+	+
Pons		
Pontine nucleus	+++	+
Median raphe nucleus	+	+
Dorsal raphe nucleus	+	+
Periaqueductal gray	+	+
Pontine reticular nucleus, oral part	+	+
Lateral lemniscus	+++	+
Rostral periolivary region	+++	+
Nucleus of the trapezoid body	+++	+
Lateral superior olive	++	+
Periolivary region	++	+
Motor trigeminal nucleus	+	+
Principal sensory trigeminal nucleus	+	+
Lateral vestibular nucleus	++	+
Cochlear nuclei	+++	+
Medulla		
Lateral paragigantocellular nucleus	+	+
Rostroventrolateral reticular nucleus	+	+
Spinal trigeminal nucleus	+	+
Dorsal motor nucleus of the vagus	++	+
Hypoglossal nucleus	+	+
Cerebellum		
Purkinje cells	+++	+
Granule cell layer	–	+
Molecular layer	–	+
Cerebellar nuclei	++	+

Level of expression: +++ high; ++ moderate; + low; – not detected.
[a] Positive cells were scattered.

results revealed that the members of the Id gene family exhibit distinct expression patterns in the adult mouse brain.

The results of the present study are tabulated (Table 2). Since the expression levels of Id1 and Id4 were low, we excluded their results from the table. The present work thus confirmed the previous observations regarding the Id2 gene expression and further demonstrated that Id2 mRNA is distributed more widely throughout the brain. Our study provides evidence that supports the involvement of Id2 in neural functions of the adult brain. In addition, the results for expression of other Id genes imply that the Id gene products play distinct but overlapping roles in the adult mouse brain. Regarding the cell types that express Id2, morphological examination of the specimens counterstained by Nissl staining suggests that most of them are neurons. However, we cannot exclude the possibility that non-neuronal cells also express Id2, depending on the brain regions, because the

present study does not include double labeling with markers for neurons.

In the limbic system, Id2 mRNA was observed in various regions including the piriform, cingulate and retrosplenial cortices, septal nucleus, hippocampus, the bed nucleus of the stria terminalis, and many amygdaloid subnuclei. In the amygdala, Id2 mRNA is expressed moderately in LaDL and LaVM and highly in intercalated cells of the amygdala. The lateral nucleus is the main input station of the amygdala for visual and auditory sensory input (Collins and Pare, 1999; McDonald, 1998), and intercalated cell masses receive inputs from the basolateral complex and project to the central nucleus (Collins and Pare, 1999). Since the amygdala is associated with emotion and behavioral responses, Id2 may play a role in regulating these neural functions.

In the developing mouse brain, Id2 mRNA expression has a boundary in the neocortical layer 5, and the boundary demarcates the transition from the sensory to motor region, suggesting that Id2 is associated with cortical regionalization (Rubenstein et al., 1999). However, in the adult brain, the boundary is not clear in our analysis (data not shown). Id2 may have some function in addition to cortical regionalization. Id2 mRNA was expressed in the cranial nerve nuclei, not only in the motor nuclei, but also the sensory nuclei. As reported previously (Andres-Barquin et al., 2000; Jen et al., 1997; Neuman et al., 1991; Rubenstein et al., 1999; Tzeng and de Vellis, 1998), Id2 mRNA was observed in neurons in the cerebral cortex and caudate putamen. In addition, most cells in the globus pallidus and pars reticulata of the substantia nigra were labeled for Id2 mRNA. These observations suggest the involvement of Id2 in motor functions.

The circadian rhythm in mammals has been thought to be under the control of the pacemaker located in the SCN of the hypothalamus (Inouye and Shibata, 1994). As reported previously (Ueda et al., 2002), Id2 mRNA was detected in SCN in our study. In addition, we found that it was also expressed in the regions of the paraventricular nucleus (PVN) and stria terminalis (BNST). Vasopressin containing pathways from the SCN serve to affect neuroendocrine and autonomic neurons in the PVN (Buijs et al., 1998). GABA and glutamate are important mediators of fast monosynaptic transmission from the SCN to defined neurons in the PVN and are candidates for conveying circadian rhythmicity to PVN regulation of neuroendocrine and autonomic processes (Hermes et al., 1996). The circadian rhythm of electrical activity in the bed nucleus of the BNST is in phase with the SCN electrical activity rhythm (Yamazaki et al., 1998). Thus, Id2 may be involved in the regulation of circadian rhythm. In accordance with this notion, Id2 expression in the SCN is high during circadian night (Ueda et al., 2002).

It is known that two regions contain neural stem cells in the adult rodent brain: the subgranular zone (SGZ) of the hippocampal dentate gyrus and the subventricular zone (SVZ) (Altman and Bayer, 1990; Doetsch et al., 1999; Eriksson et al., 1998; Goldman, 1998; Johansson et al., 1999). The SGZ is the source of granule cells in the hippocampus produced during the juvenile and adult periods (Altman and Bayer, 1990), and the anterior part of the subventricular zone (SVZa) is a source of neuronal progenitor cells for the olfactory bulb (Luskin, 1993). In this study, we found that Id2 mRNA was expressed in the SVZa. Id2 may be related to the production of neurons in the olfactory bulb. This notion is consistent with the physiological activity of Id proteins because Id proteins are thought to function to expand and maintain the immature cells.

Acknowledgments

We are grateful to M. Sato for sharing equipment and D. Nathans and F. Sablitzky for materials. This work was supported by Grants-in-Aid and by the 21st Century COE program "Biomedical Imaging Technology Integration Program" from the Japan Society for the Promotion of Science.

REFERENCES

Altman, J., Bayer, S.A., 1990. Migration and distribution of two populations of hippocampal granule cell precursors during the perinatal and postnatal periods. J. Comp. Neurol. 301, 365–381.

Andres-Barquin, P.J., Hernandez, M.C., Israel, M.A., 2000. Id genes in nervous system development. Histol. Histopathol. 15, 603–618.

Benezra, R., Davis, R.L., Lockshon, D., Turner, D.J., Weintraub, H., 1990. The protein Id: a negative regulator of helix–loop–helix DNA binding proteins. Cell 61, 49–59.

Buijs, R.M., Hermes, M.H., Kalsbeek, A., 1998. The suprachiasmatic nucleus–paraventricular nucleus interactions: a bridge to the neuroendocrine and autonomic nervous system. Prog. Brain Res. 119, 365–382.

Christy, B.A., Sanders, L.K., Lau, L.F., Copeland, N.G., Jenkins, N.A., Nathans, D., 1991. An Id-related helix–loop–helix protein encoded by a growth factor-inducible gene. Proc. Natl. Acad. Sci. U. S. A. 88, 1815–1819.

Collins, D.R., Pare, D., 1999. Reciprocal changes in the firing probability of lateral and central medial amygdala neurons. J. Neurosci. 19, 836–844.

Doetsch, F., Caille, I., Lim, D.A., Garcia-Verdugo, J.M., Alvarez-Buylla, A., 1999. Subventricular zone astrocytes are neural stem cells in the adult mammalian brain. Cell 97, 703–716.

Elliott, R.C., Khademi, S., Pleasure, S.J., Parent, J.M., Lowenstein, D. H., 2001. Differential regulation of basic helix–loop–helix mRNAs in the dentate gyrus following status epilepticus. Neuroscience 106, 79–88.

Eriksson, P.S., Perfilieva, E., Bjork-Eriksson, T., Alborn, A.M., Nordborg, C., Peterson, D.A., Gage, F.H., 1998. Neurogenesis in the adult human hippocampus. Nat. Med. 4, 1313–1317.

Goldman, S.A., 1998. Adult neurogenesis: from canaries to the clinic. J. Neurobiol. 36, 267–286.

Hermes, M.L., Coderre, E.M., Buijs, R.M., Renaud, L.P., 1996. GABA and glutamate mediate rapid neurotransmission from suprachiasmatic nucleus to hypothalamic paraventricular nucleus in rat. J. Physiol. 496, 749–757.

Inouye, S.T., Shibata, S., 1994. Neurochemical organization of circadian rhythm in the suprachiasmatic nucleus. Neurosci. Res. 20, 109–130.

Ishii, K., Oda, Y., Ichikawa, T., Deguchi, T., 1990. Complementary DNAs for choline acetyltransferase from spinal cords of rat and mouse: nucleotide sequences, expression in mammalian cells, and in situ hybridization. Brain Res. Mol. Brain Res. 7, 151–159.

Jen, Y., Manova, K., Benezra, R., 1996. Expression patterns of Id1, Id2, and Id3 are highly related but distinct from that of Id4 during mouse embryogenesis. Dev. Dyn. 207, 235–252.

Jen, Y., Manova, K., Benezra, R., 1997. Each member of the Id Gene family exhibits a unique expression pattern in mouse gastrulation and neurogenesis. Dev. Dyn. 208, 92–106.

Johansson, C.B., Momma, S., Clarke, D.L., Risling, M., Lendahl, U., Frisen, J., 1999. Identification of a neural stem cell in the adult mammalian central nervous system. Cell 96, 25–34.

Kageyama, R., Nakanishi, S., 1997. Helix–loop–helix factors in growth and differentiation of the vertebrate nervous system. Curr. Opin. Genet. Dev. 7, 659–665.

Luskin, M.B., 1993. Restricted proliferation and migration of postnatally generated neurons derived from the forebrain subventricular zone. Neuron 11, 173–189.

Massari, M.E., Murre, C., 2000. Helix–loop–helix proteins: regulators of transcription in eucaryotic organisms. Mol. Cell. Biol. 20, 429–440.

McDonald, A.J., 1998. Cortical pathways to the mammalian amygdala. Prog. Neurobiol. 55, 257–332.

Mori, S., Nishikawa, S.I., Yokota, Y., 2000. Lactation defect in mice lacking the helix–loop–helix inhibitor Id2. EMBO J. 19, 5772–5781.

Neuman, T., Keen, A., Zuber, M.X., Kristjansson, G.I., Gruss, P., Nornes, H.O., 1991. Neuronal expression of regulatory helix–loop–helix factor Id2 gene in mouse. Dev. Biol. 160, 186–195.

Paxinos, G., Franklin, K., 2001. The Mouse Brain in Stereotaxic Coordinates, 2nd ed. Academic Press, San Diego, CA.

Riechmann, V., van Cruchten, I., Sablitzky, F., 1994. The expression pattern of Id4, a novel dominant negative helix–loop–helix protein, is distinct from Id1, Id2 and Id3. Nucleic Acids Res. 22, 749–755.

Rubenstein, J.L.R., Anderson, S., Shi, L., Miyashita-Lin, E., Bulfone, A., Hevner, R., 1999. Genetic control of cortical regionalization and connectivity. Cereb. Cortex 9, 524–532.

Ruzinova, M.B., Benezra, R., 2003. Id proteins in development, cell cycle and cancer. Trends Cell Biol. 12, 410–418.

Tzeng, S.F., de Vellis, J., 1998. Id1, Id2, and Id3 gene expression in neural cells during development. Glia 24, 372–381.

Ueda, H.R., Chen, W., Adachi, A., Wakamatsu, H., Hayashi, S., Takasugi, T., Nagano, M., Nakahama, K., Suzuki, Y., Sugano, S., Iino, M., Shigeyoshi, Y., Hashimoto, S., 2002. A transcription factor response element for gene expression during circadian night. Nature 418, 534–539.

Yamazaki, S., Kerbeshian, M.C., Hocker, C.G., Block, G.D., Menaker, M., 1998. Rhythmic properties of the hamster suprachiasmatic nucleus in vivo. J. Neurosci. 18, 10709–10723.

Yokota, Y., Mori, S., 2002. Role of Id family proteins in growth control. J. Cell. Physiol. 190, 21–28.

ELSEVIER

Journal of the Neurological Sciences 247 (2006) 109–111

Journal of the Neurological Sciences

www.elsevier.com/locate/jns

Short communication

Epileptic polyopia with right temporal lobe epilepsy as studied by FDG-PET and MRI: A case report

Takahiro Mitsueda-Ono [a], Akio Ikeda [a,*], Eri Noguchi [a], Shigetoshi Takaya [b], Hidenao Fukuyama [b], Shun Shimohama [a], Ryosuke Takahashi [a]

[a] *Department of Neurology, Kyoto University Hospital, 54 Shogoin-Kawaharacho, Sakyo-ku, Kyoto 606-8507, Japan*
[b] *Human Brain Research Center, Kyoto University School of Medicine, Japan*

Received 30 December 2005; received in revised form 14 April 2006; accepted 18 April 2006
Available online 21 June 2006

Abstract

Polyopia is one of rare, visual hallucinations. A 61-year-old man suffered from daily episodes of polyopia and generalized convulsions, and he was diagnosed as right temporal lobe epilepsy. MRI revealed right amygdalar swelling. FDG-PET showed hypometabolism in the right anterior temporal and the mesial occipital areas. Polyopia is thought to be caused by dysfunction of updating process of visual information in the visual association cortices. It was most likely that, in this patient, both mesial temporal and ipsilateral occipital areas were responsible for manifesting epileptic polyopia, as ictal onset zone and symptomatogenic zone, respectively.

Keywords: Polyopia; Partial epilepsy; Amygdala; FDG-PET

1. Introduction

Polyopia is one of complex visual hallucinations, manifesting appearance of plural images as erroneous visual perceptions even after the object has left out of visual field. On the other hand, palinopsia is also a kind of visual hallucinations, appearing plenty of the same images while watching one object [1]. Since this report, it was frequently reported referring to several neurological disorders, but it seems to involve temporo-occipital area commonly.

On the other hand, human "amygdalar epilepsy" is not established yet [2]. Amongst a series of 174 cases with intractable temporal lobe epilepsy (TLE) confirmed by video EEG monitoring, amygdalar enlargement was observed in seven patients (4%) [3].

Abbreviations: EEG, electroencephalography; MRI, magnetic resonance image; FDG, fluorodeoxyglicose; PET, positron emission computed tomography; TLE, temporal lobe epilepsy; AVM, artery venous malformation; FLAIR, fluid-attenuated inversion recovery.

Corresponding author. Tel.: +81 75 751 3772; fax: +81 75 751 9416.
E-mail address: akio@kuhp.kyoto-u.ac.jp (A. Ikeda).

0022-510X/$ - see front matter © 2006 Elsevier B.V. All rights reserved.
doi:10.1016/j.jns.2006.04.010

This is the first report that mentioned amygdalar enlargement and interictal PET study in epilepsy patients having polyopia. It may suggest that amygdala is also involved in manifesting polyopia as the ictal onset zone, but not necessarily as the symptomatogenic zone.

2. Case report

A 61-year-old right-handed man, without history of febrile convulsions, any developmental problems or head injury, was admitted because he had very frequent episodes of seeing "multiple, identical images previously seen" (called as polyopia as explained below) that were overlapped on his real vision mainly on the left side. He had several episodes of generalized convulsions with tongue bite since the age of 47 years, and he was free from generalized convulsions in the last 14 years, but the current type of visual symptoms started since age 60 years. Frequency of the current attacks has increased from once per 2 or 3 days to several times per day.

The polyopia episodes were elaborated as follows. He saw multiple, same persons who had been seen just before;

he had an episode while playing an aerobic dance and saw multiple same persons in front of him in a row who were actually playing side to him. On the other occasions, he saw some people around him whom he could not identify, and the experienced scene was accompanied. He felt as if he was moving along these people in the scene (Fig. 1), followed by ascending sensation of numbness on his trunk bilaterally. Each episode lasted about 10 s, and initially he was aware and he thought that he did not lose his consciousness. One of the authors witnessed the episode when he showed incoherent vocalization, oral and hand automatisms, no responsiveness and test words given during the episode were not remembered, being consistent with simple partial seizures followed by complex partial seizures. Once the visual symptoms started, he felt angry against and wanted to quit or overcome the episodes; otherwise, other emotional symptoms were not accompanied.

He has no family history of neurological diseases. General and neurological examinations revealed no abnormality in the interictal period. Interictal EEG showed intermittent irregular slow (2.5 to 3 Hz) activity in the right fronto-temporal area, and several sharp transients in the right midtemporal area once per several minutes. Ictal EEG was not recorded.

The right amygdala increased in size on MRI (Fig. 2a and b), and there were no gadolinium-enhanced lesions. The intensity in FLAIR images was not increased. Neither hippocampal atrophy nor sclerosis was detected on both sides. In FDG-PET study, there was regional glucose hypometabolism in the right temporal and in the caudal part along the calcarine fissure in the right medial occipital area (Fig. 3). As compared with healthy subjects by using SPM, regional glucose hypometabolism was significant in the right temporo-occipital area.

All neuropsychological examinations resulted in normal limits as follows: Wechsler Memory Scale: verbal 96, visual 117, general 103, attention 106, delay 96; Western Aphasia Battery: AQ 100, CQ 99.4; Raven's colored progressive matrices test: 32/37; Boston Naming Test: 48/60; Wechsler

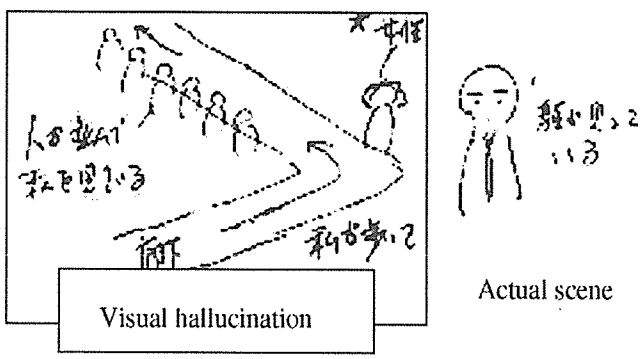

Fig. 1. One example of the polyopia drawn by the patient. While facing the doctor to whom he was talking, suddenly he felt as if he was walking along the corridor. Besides, he saw a row of the same unidentified persons and an unidentified woman who he just met before along the corridor. This visual hallucination appeared in the left visual field.

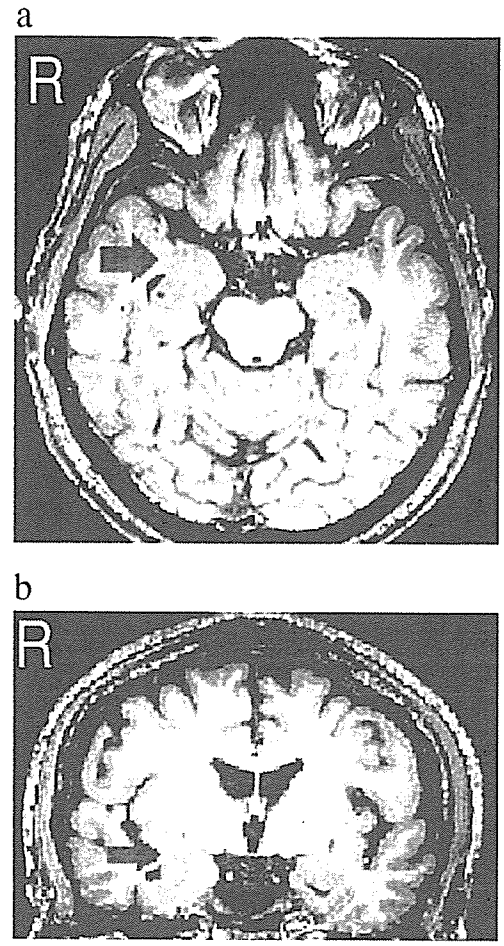

Fig. 2. T1-weighed MRI images. Right amygdalar enlargement was found in the axial (a) and the coronal (b) images. Arrow shows the enlarged amygdala.

Adult Intelligence Scale-Revised: verbal IQ 131, performance IQ 136, total IQ 136.

We diagnosed him as right TLE based on ictal semiology, EEG, MRI and FDG-PET, and thus carbamazepine was started. It was gradually increased up to 300 mg/day, and his ictal symptoms have completely stopped.

3. Discussion

There were several reports that mentioned polyopia as seen in the present patient until now; however, it was rarely reported. According to those reports, it was observed in patients with cerebral infarction [1], head trauma [4], AVM [5], multiple sclerosis [6], non-ketoacidotic hyperglycemia [7], Creutzfeldt-Jakob disease [8] and migraine [9]. In case of partial epilepsy, occipitotemporal region or hippocampus was responsible [10].

From stimulation study, simple visual hallucination (e.g., light or scotoma) occurred by the stimulation of area 18 or 19 [11]. Lateral temporal lobe correlates with playback of sensory input. Stimulation of this region reminded patients of previously experienced scene [11].

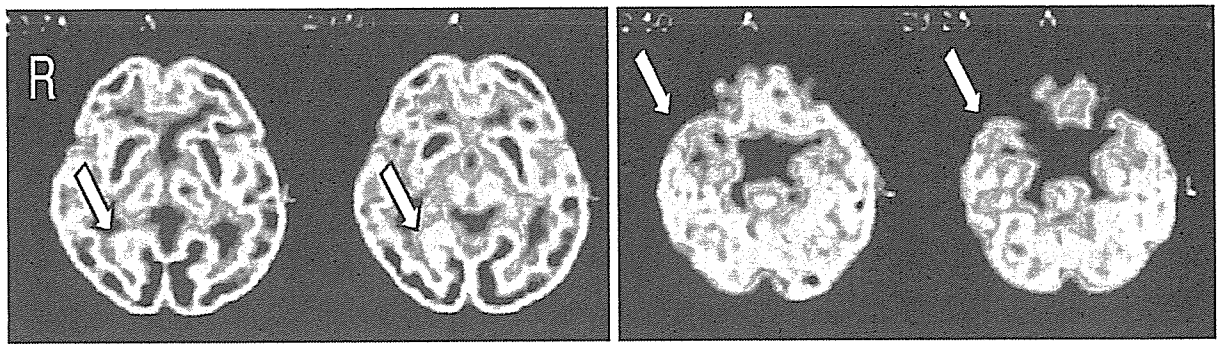

Fig. 3. PET study revealed hypometabolism in the right temporal lobe and right mesial occipital area (as shown by arrows).

In order to constitute polyopia, dysfunction of updating ongoing spatial perception in response to the circumstances would be necessary. It could occur by the impairment of not primary visual cortex but lateral temporal lobe, which correlates to record and accumulate visual perception. The responsible area for polyopia has remained unsolved; however, the abnormal input to the visual association cortex located in the temporo-occipito-parietal area could be one of the causes [12].

In the present patient, both right anterior temporal and mesial occipital areas were involved according to FDG-PET study. Hypometabolic brain areas as revealed by FDG-PET indicate not only epileptogenic but also symptomatogenic brain regions [13]. Hence, these two regions are involved as either symptomatogenic or epileptogenic zone. Right anterior temporal area (frequent interictal spikes in interictal EEG), especially the swollen right amygdala, most likely plays an important role as epileptogenic zone.

Amygdalar enlargement is a distinct entity from mesial temporal sclerosis. When we consider medial temporal lobe epilepsy, it is necessary to pay attention to amygdalar abnormality. Abnormal EEG discharges with amygdalar enlargement that acts as epileptogenic zone can lead to ipsilateral occipital area as symptomatogenic zone. This finding also suggests the connection between amygdala and occipital lobe. Additionally, it is also noteworthy that polyopia can manifest even in patients with TLE since an epileptogenic zone could be distant from the symptomatogenic zone of polyopia.

Acknowledgement

This study was supported by the Research Grant for the Treatment of Intractable Epilepsy (16-1) from the Japan Ministry of Health, Labor and Welfare, and a Scientific Research Grant (C2) 18590935 from the Japan Society for Promotion of Sciences.

References

[1] Critchley M. Types of visual preservation: "palinopsia" and "illusory visual spread". Brain 1951;74:267–99.
[2] Wieser HG. Mesial temporal lobe epilepsy versus amygdalar epilepsy: late seizure recurrence after initially successful amygdalotomy and regained seizure control following hippocampectomy. Epileptic Disord 2000;2:141–51.
[3] Bower SPC, Vorgin SJ, Morris K, Cox I, Murphy M, Kilpatrick CJ, et al. Amygdala volumetry in "imaging-negative" temporal lobe epilepsy. J Neurol Neurosurg Psychiatry 2003;74:1245–9.
[4] Kinsbourne M, Warrington EK. A study of visual preservation. J Neurol Neurosurg Psychiatry 1963;26:468–75.
[5] Jacobs L. Visual allesthesia. Neurology 1980;30:1059–63.
[6] Jacome DE. Palinopsia and bitemporal visual extinction on fixation. Ann Ophthalmol 1985;17:251–2.
[7] Johnson SF, Loge RV. Palinopsia due to nonketotic hyperglycemia. West J Med 1988;148:331–2.
[8] Purvin V, Bonnin J, Goodman J. Palinopsia as a presenting manifestation of Creutzfeldt-Jacob disease. J Clin Neuroophthalmol 1989;9:242–8.
[9] Klee A, Willanger R. Disturbances of visual perception in migraine: review of the literature and a report of eight cases. Acta Neurol Scand 1966;42:400–14.
[10] Christian GB, Felix OB, Horst U, Johannes S, Martin K, Christian EE. Localizing value of epileptic visual auras. Brain 2000;123:244–53.
[11] Penfield W, Perot P. The brain's record of auditory and visual experience. Brain 1963;86:596–696.
[12] Okada K, Akamatsu N, Hashimoto T, Uozumi T, Tsuji S. A case of right mesial temporal lobe epilepsy accompanied with ictal polyopsia. Clin Neurol 2004;44:39–42 [Only abstract written in English].
[13] Schlaug G, Antke C, Holthausen H, Arnold S, Ebner A, Tuxhorn I, et al. Ictal motor signs and interictal regional cerebral hypometabolism. Neurology 1997;49:341–50.

ELSEVIER

Clinical Neurophysiology 117 (2006) 1481–1486

www.elsevier.com/locate/clinph

Generators and temporal succession of giant somatosensory evoked potentials in cortical reflex myoclonus: Epicortical recording from sensorimotor cortex

Takefumi Hitomi [a], Akio Ikeda [a,*], Riki Matsumoto [a], Masako Kinoshita [a], Junya Taki [b], Keiko Usui [c], Nobuhiro Mikuni [b], Takashi Nagamine [c], Nobuo Hashimoto [b], Hiroshi Shibasaki [d], Ryosuke Takahashi [a]

[a] *Department of Neurology, Kyoto University Graduate School of Medicine, Kyoto, Japan*
[b] *Department of Neurosurgery, Kyoto University Graduate School of Medicine, Kyoto, Japan*
[c] *Department of Brain Pathophysiology, Human Brain Research Center, Kyoto University Graduate School of Medicine, Kyoto, Japan*
[d] *Takeda General Hospital, Kyoto, Japan*

Accepted 29 March 2006

Abstract

Objective: To clarify the generator mechanism of giant somatosensory evoked potentials (giant SEPs) and the hyperexcitability of primary somatosensory and motor cortices (SI and MI).

Methods: In a patient with intractable focal seizures manifesting cortical reflex myoclonus of the left foot, giant SEPs to left tibial nerve stimulation were epicortically recorded as a part of presurgical evaluation with subdural electrodes.

Results: In the single pulse SEPs, enlarged P1–N1 components were observed at the foot area of the SI and MI (86.5–258.8 μV, respectively), and the peak latencies were always shorter at SI than at MI by 6 ms. Similar findings were obtained for peroneal and sural nerve stimulation. In the paired pulse SEPs, the second response was less suppressed, as compared to other interstimulus intervals (ISIs), with ISIs of 40 and 200 ms both at SI and MI.

Conclusions: In this particular patient, cortical hyperexcitability to somatosensory stimuli seems to originate from SI but subsequently both SI and MI are responsible for the generation of giant SEPs and cortical reflex myoclonus.

Significance: Somatosensory and primary motor cortices both generated enhanced early cortical components of SEPs, most likely by enhancing the latter by the former.

Keywords: Giant somatosensory evoked potential (giant SEP); Cortical reflex myoclonus; Primary somatosensory cortex (SI); Primary motor cortex (MI)

1. Introduction

Extremely enlarged cortical components of somatosensory evoked potentials (giant SEPs) are observed in the majority of patients with cortical reflex myoclonus. The giant SEPs are considered to represent the degree of cortical hyperexcitability of the primary sensorimotor cortices (SMI) in response to somatosensory stimuli (Shibasaki et al., 1985), and are considered to result from pathological enhancement of certain early components of normal SEPs (Ikeda et al., 1995; Kakigi and Shibasaki, 1987a; Shibasaki

Abbreviations: SEP, somatosensory evoked potential; SMI, primary sensorimotor cortices; SI, primary somatosensory cortex; MI, primary motor cortex; ISI, interstimulus interval; SEP-R, SEP recovery function; ECoG, electrocorticogram; MEG, magnetoencephalography; SEF, somatosensory evoked magnetic field.

* Corresponding author. Address: Department of Neurology, Kyoto University Hospital, 54 Shogoin-Kawaharacho, Sakyo-ku, Kyoto 606-8507, Japan. Tel.: +81 75 751 3772; fax: +81 75 751 9416.

E-mail address: akio@kuhp.kyoto-u.ac.jp (A. Ikeda).

1388-2457/$30.00
doi:10.1016/j.clinph.2006.03.029

et al., 1990). As for the generator mechanism of giant SEPs, previous study by means of simultaneous recording of SEPs and somatosensory evoked magnetic fields (SEFs) showed that abnormal hyperexcitability involves both primary somatosensory and motor cortices (SI and MI, respectively) (Mima et al., 1998). However, the generator sources of giant SEPs have not been fully understood.

In the present study, we investigated the giant SEPs recorded from chronically implanted subdural electrodes in order to clarify the generator mechanism and the hyperexcitability of SI and MI in a patient with intractable focal epilepsy manifesting cortical reflex myoclonus. Only the abstract for this objective appeared elsewhere (Hitomi et al., 2004), and other electrophysiological and clinical features of the patient are described elsewhere for an entirely different purpose (Matsumoto et al., 2005; Mikuni et al., 2005; Nakagawa et al., in press).

2. Patient and methods

A 31-year-old man had intractable focal seizures and cortical reflex myoclonus involving the left foot due to focal cortical dysplasia in the right parasagittal central region. The patient was on many kinds of anticonvulsants, such as carbamazepine (800 mg/day), phenytoin (300 mg/day), phenobarbital (80 mg/day), zonisamide (700 mg/day) and clobazam (10 mg/day). By video-EEG monitoring, the epileptogenic zone was defined at and very close to the foot area of the right SI and MI. Clinically he had both positive and associated negative myoclonus and showed an enhanced long-loop transcortical reflex (C-reflex) to electrical stimulation of the left foot. Before implantation of the subdural electrodes, SEFs in response to stimulation of bilateral tibial nerves were recorded (passband: 0.07–200 Hz, sampling rate: 901 Hz) in the magnetically shielded room with the 122 first-order planar SQUID gradiometers (Neuromag122, Neuromag, Helsinki, Finland).

2.1. Scalp SEPs

Scalp SEPs in response to stimulation of bilateral tibial and sural nerves were recorded before implantation of the subdural electrodes and 20 days after the resective surgery. The electrical stimulus was presented as a constant voltage square-wave pulse of 0.2 ms duration, and interstimulus interval (ISI) was set to 2.9 s. It was delivered to the tibial nerve at the ankle and to the sural nerve below the lateral malleolus. Stimulus intensity was adjusted to 120% of motor threshold so as to produce a clear twitch of the hallux for the tibial nerve and to 300% of sensory threshold for the sural nerve. The scalp electrodes were placed at Fz, Cz and Pz based on the 10–20 International System, and were also placed at CPz, CP3 and CP4 defined as the midway between each corresponding pair of electrodes. All electrodes were referred to the linked earlobes (A1 + A2). The bandpass filter of the amplifier was set to 1.6–3000 Hz, and sampling rate was set to 10,000 Hz. Three hundred responses for each session were averaged and at least two sets were recorded to confirm the reproducibility of the waveforms.

2.2. Epicortical SEPs

Single and paired pulse SEPs were recorded from subdural electrodes while the patient was undergoing invasive seizure monitoring and functional mapping. Informed consent was obtained based on the Clinical Research Protocol No. 79, approved by the Committee of Medical Ethics, Kyoto University Graduate School of Medicine. Single pulse SEPs were recorded by stimulation of the left tibial, peroneal and sural nerves. The condition of electrical stimulation for the left tibial and sural nerves were the same as those for the scalp SEP recording except for shorter ISI (1 s) in the epicortical recording. As for the left peroneal nerve, stimulus was delivered on the skin over the left fibular head and stimulus intensity was adjusted to 120% of motor threshold of the tibialis anterior muscle. All subdural electrodes were referred to the skin electrode on the left mastoid process. All other recording conditions were the same as those for scalp SEP recording.

Recovery functions of SEP response were studied by giving paired stimuli with various ISIs. Each pair of stimuli was delivered once every 3 s or longer. ISIs were set to 30, 40, 60, 80, 100, 120, 140, 160 and 200 ms. In order to maintain the same recording condition among different ISIs, stimuli with different ISIs were randomly delivered in the same recording session, and the single pulse stimuli were also intermixed among them. The SEP recovery function (SEP-R) of P1–N1 and N1–P2 components of the response to the second stimuli (SEP2) was calculated with respect to the response to the first stimuli (SEP1) for each ISI. Cortical excitability was judged to be non-suppressed when the ratio of SEP2/SEP1 was 100% or larger for both SI and MI. For statistical analysis, the Mann–Whitney U test was employed to compare the ratio of SEP2/SEP1 between non-suppressed ISIs data and suppressed one. The level of significance was set with P value of less than 5%.

3. Results

3.1. Scalp SEPs

Scalp SEPs following the left tibial nerve stimulation showed maximal cortical responses at CPz. As for the latencies, peaks of SEPs to the left foot stimulation were delayed (P1: 51.6 ms, N1: 63.8 ms and P2: 103.0 ms) as compared with the right foot stimulation (P1: 42.7 ms, N1: 55.8 ms and P2: 65.4 ms) (Table 1A, Fig. 1A and B). With regard to the amplitudes, P1–N1 and N1–P2 components for the left foot stimulation (P1–N1: 15.0 uV and N1–P2:

Table 1

Nerve	Electrode	Latency (ms)			Amplitude (μV)		
		P1	N1	P2	Baseline-P1	P1–N1	N1–P2
A scalp SEP							
Left tibial	CPz	51.6	63.8	103.0	6.0	15.0	17.1
Right tibial	CPz	42.7	55.8	65.4	0.1	3.6	2.7
Left sural	CPz	54.6	70.2	158.5	2.2	9.7	17.1
Right sural	CPz	50.1	61.4	135.0	0.1	3.0	8.6
B subdural SEP							
Left tibial	A19 (SI)	45.0	59.5	73.2	46.2	207.2	152.3
	B3 (MI)	49.6	64.8	82.4	2.4	86.5	86.6
Left peroneal	A19 (SI)	38.1	51.6	83.5	14.0	125.5	156.1
	B3 (MI)	43.8	59.9	88.2	47.3	258.8	276.8
Left sural	A19 (SI)	43.5	62.1	95.2	25.9	120.8	92.9
	B3 (MI)	49.1	68.7	97.2	32.0	104.5	102.1

17.1 μV) were about 4 times larger than those for the right foot stimulation (P1–N1: 3.6 μV and N1–P2: 2.7 μV) (Table 1A, Fig. 1A and B). P1–N1 for the left tibial nerve stimulation was compatible with 'giant' SEPs according to the previous study (P1–N1 amplitude being more than 11.4 μV (mean+3SD)) (Kakigi and Shibasaki, 1987b). As for the sural nerve stimulation, cortical components also showed delayed latencies and increased amplitudes to the left foot stimulation as compared with the right foot stimulation (Table 1A).

Twenty days after the resective surgery, scalp SEPs were recorded again. As for SEPs to the left tibial nerve stimulation, peak latencies (P1: 53.4 ms, N1: 70.2 ms and P2: 108.3 ms) were still delayed and amplitude of P1–N1 component (11.2 μV) was larger than that for the contralateral stimulation (2.4 μV). However, its amplitude

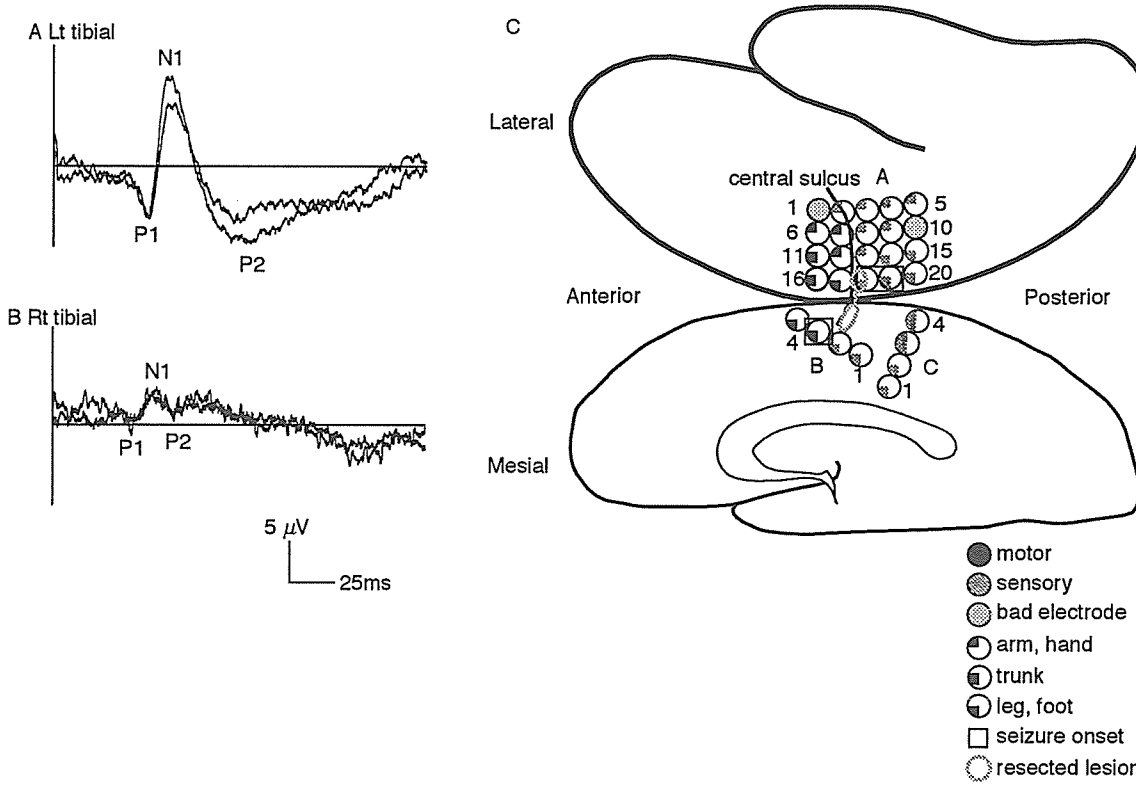

Fig. 1. Scalp recorded SEP waveforms at CPz to the left (A) and right (B) tibial nerve stimulation and the results of invasive functional mapping (C). In C, cortical functions beneath each subdural electrode are shown by symbols. B3, A18 and A19, as surrounded by bold squares, were defined as seizure onset area. Interictal spikes were frequently recorded at B2, B3, A18 and A19. A17, B3 and B4 corresponded to the foot or leg motor cortex, and A14, 15, 18-20, B1, 2 and C 1–4 corresponded to that of sensory cortex as determined by electrical stimulation. Gray bold circle and line indicated that the resected epileptogenic area of the cortical dysplasia was located in the posterior portion of the post-central gyrus reaching to the bottom of the right central sulcus.

became smaller in spite of the presence of craniotomy as compared with one before surgery.

As for the comparison between the scalp SEPs and SEFs to the left tibial nerve stimulation, peak latencies of P1 and N1 components at CPz were similar to those of SEFs (P1: 50.4 ms, N1: 62.4 ms).

3.2. Epicortical SEPs

Enhanced cortical components were recorded at A18 and A19 (SI) and at B3 (MI) (Fig. 1C). SEP waveforms among the 3 stimulated nerves (tibial, peroneal and sural) were similar in the latency of P1 and N1, and P1–N1 amplitude was equally enlarged (Table 1B). The peak latencies of the left peroneal nerve SEPs were shorter by 5–7 ms than those of tibial and sural nerve SEPs, since the former was stimulated at the fibular head whereas the latter two were stimulated at the ankle.

There was a consistent latency difference of each peak between SI and MI, although the waveforms of cortical components at SI (A19) and MI (B3) were similar (Fig. 2). Peak latencies of each component (P1, N1, P2) at SI (A19) were shorter than those at MI (B3) by about 6 ms on average (mean ± SD: 5.8 ± 2.1; ranging from 2.0 to 9.2); left tibial (6.4 ± 2.8; 4.6–9.2), peroneal (4.7 ± 2.4; 2.0–5.6) and sural (6.2 ± 1.9; 4.7–8.3). Peak latencies at SI (B2) were also shorter than those at MI (B3) by about 6 ms (6.0 ± 2.3; 2.0–9.9) despite the proximity of the recording site (Fig. 2). The P1–N1 amplitudes at both SI (A19) and MI (B3) were equally enhanced for the left tibial, peroneal and sural nerve stimulation (Table 1B).

The comparison between scalp and epicortical SEPs to the left tibial nerve stimulation showed similar morphology of P1 and N1 components, but the late components including P2 were different (Fig. 2A). A similar tendency was observed for the left sural nerve stimulation (Fig. 2B). Peak latencies of P1 and N1 components at CPz were longer than those at SI (A19) by about 4–11 ms to the left tibial (P1: 6.6 ms, N1: 4.3 ms) and sural (P1: 8.1 ms, N1: 11.1 ms) nerve stimulation. By contrast, the time difference between MI (B3) and CPz was much less than that between SI and CPz; left tibial (P1: 2.0 ms, N1: 1.0 ms) and sural (P1: 5.5 ms, N1: 1.5 ms) nerve stimulation (Table 1, Fig. 2).

As for the SEP-R of P1–N1 and N1–P2 components, the SEP2 was less than 100% of the SEP1 at SI (A19) and MI (B3) with all the ISIs examined in the present study (Fig. 3), as judged by normal range (within mean ± 3SD of those obtained from normal subjects) in previous scalp-recorded, paired SEP study (Ugawa et al., 1991). In detail, the SEP2 was less than 60% of the SEP1 at SI (A19) and MI (B3) at ISI of 30–200 ms except for the ISIs of 40 ms (80.7% at SI and 92.0% at MI for P1–N1 component, 94.5% at SI and 82.4% at MI for N1–P2 component) and of 200 ms (77.2% at SI and 63.0% at MI, 94.5% at SI and 91.3% at MI) (Fig. 3). The degree of

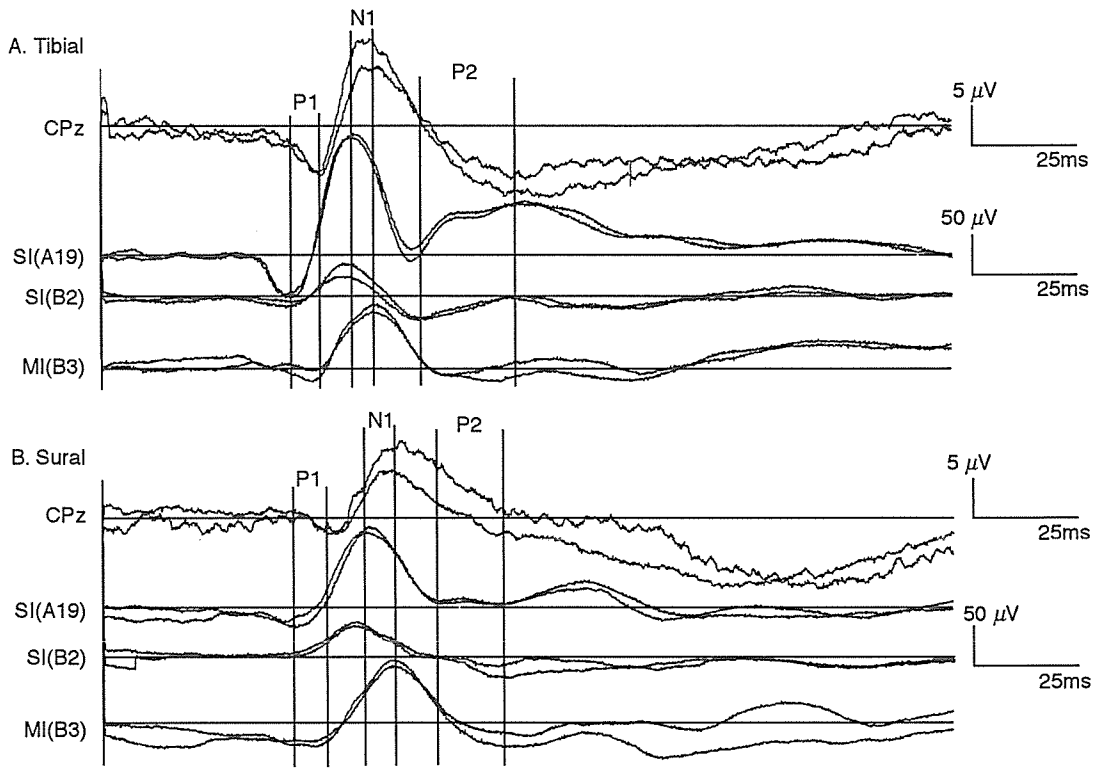

Fig. 2. Scalp (CPz) and subdurally (SI and MI) recorded SEPs to the left tibial (A) and sural (B) nerve stimulation. Vertical solid lines show peaks of each component (P1, N1, P2) at CPz and vertical dotted lines show those at SI (A19 and B2) to the left tibial and sural nerve stimulation. The peak latencies were consistently longer at MI as compared with SI, and the latencies at MI were similar to those at CPz.

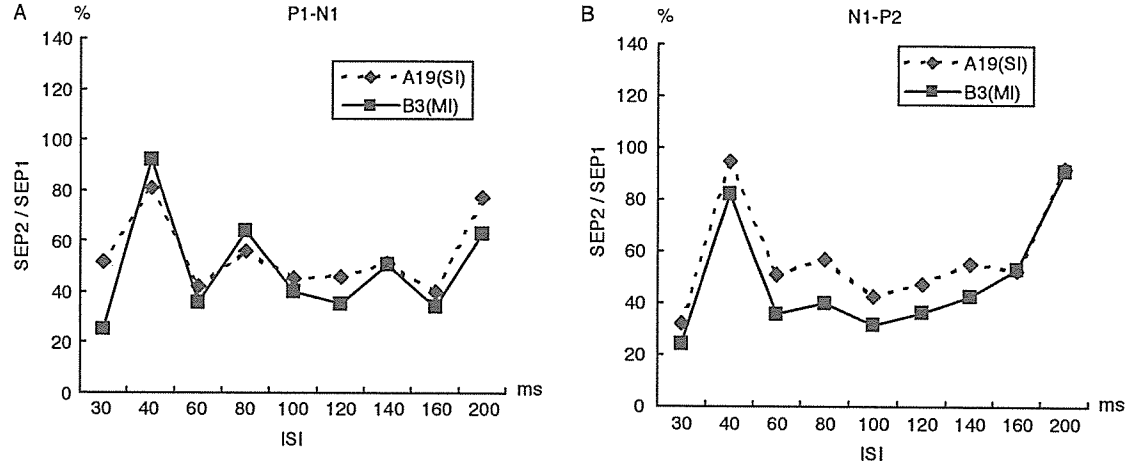

Fig. 3. Recovery curve of P1–N1 (A) and N1–P2 (B) components of the subdurally recorded SEP amplitude in the paired pulse stimulation paradigm. Dotted lines; recovery curve at A19 (SI), solid lines; recovery curve at B3 (MI). The second response was significantly less suppressed at ISIs of 40 and 200 ms, as compared with other ISIs, for P1–N1 and N1–P2 components both at SI and MI.

suppression of SEP 2 at ISIs of 40 and 200 ms (labeled as less suppressed) was significantly different as compared with that of other ISIs (labeled as suppressed) (P1–N1 component: $P=0.004$, N1–P2 component: $P=0.003$).

4. Discussion

With regard to the upper limb stimulation, Cowan et al. recorded intraoperative epicortical giant SEPs under general anesthesia (Cowan et al., 1986). They showed that the latency and polarity of the SEP waveforms, recorded from the cortex apparently posterior to the postcentral gyrus, were similar to those of the scalp recorded ones, although EEG and electrocorticogram (ECoG) were not simultaneously recorded (Cowan et al., 1986). However, there was no previous report of giant SEPs recorded while awake, and furthermore, no studies recorded directly from SI and MI simultaneously. To our knowledge, this is the clear invasive recording of giant SEPs at both SI and MI following lower limb stimulation in an awake patient with cortical reflex myoclonus, and thus it enables us to investigate at least a part of the mechanism underlying generation of cortical reflex myoclonus. However, we should consider two technical limitations in this study. First, some part of the left foot/leg SMI was not covered by the subdural electrodes. Second, the influence of cortical dysplasia or epileptic hyperexcitability on giant SEP generation could not be excluded.

Giant SEPs recorded from SI and MI were similar in morphology. These findings indicate that both SI and MI are hyperexcitable to somatosensory stimuli. The fact that the peaks at SI always occurred earlier than those at MI by about 6 ms suggests that, in the present patient, enhanced response to somatosensory input initially occurred in SI due to its own hyperexcitability, and subsequently the impulse is conducted to MI. The delay of 6 ms seems consistent with cortico-cortical conduction time, since conduction time of a similar duration have been recorded between different muscles within MI in cortical myoclonus (Brown et al., 1991).

Therefore, giant SEPs in this patient are composed of two components; one due to SI hyperexcitability causing giant response to the somatosensory input, and the other arising from MI hyperexcitability most likely induced by the input from SI. This hyperexcitability enhanced by SI, in the present patient, was supported by the fact that SI was the most usual source of the pre-myoclonus spike in patients with cortical reflex myoclonus (Uesaka et al., 1996), but it may not completely exclude the possibility that MI itself is hyperexcitable. Although there is a direct input from the thalamus to the motor cortices and MI alone could also be the source of the pre-myoclonus spike in some patients with cortical myoclonus (Terao et al., 1997; Uesaka et al., 1996), the present findings do not suggest the role of this system at least in the present case. Previous magnetoencephalographic (MEG) study on cortical reflex myoclonus suggested the hyperexcitability of both SI and MI, but the time difference between SI and MI was not clearly delineated (Mima et al., 1998). It may be explained by the limited sensitivity of MEG as compared with epicortical recording or by the different etiology between the two disease groups.

The similar morphology of early components of giant SEPs between scalp and epicortical recording is consistent with the previous upper limb study (Cowan et al., 1986). However, the peaks P1 and N1 occurred consistently earlier at subdural SI than over the scalp by 4.3–11.1 ms. It could be explained, at least partly, by the phase shift of about 8 ms as the effect of skull bone which could behave as the 15 Hz high frequency filter (Tyner et al., 1983). On the other hand, P1 and N1 peaks at subdural MI were similar to those at scalp recording. Foot MI was buried in the mesial surface whereas foot SI was exposed both on the lateral and mesial surfaces as shown in Fig. 1C. Taken together with the skull bone effect as described above, it is postulated that scalp recorded P1 and N1 reflect those arising from SI rather than MI in the present

patient. In contrast, the morphology of the late components (including P2) of giant SEPs was not identical between the scalp EEG and the ECoG. It may be explained by the different position of reference electrodes and different ISI employed between the scalp and ECoG recording (the former adopted linked earlobes as the reference and ISI of 2.9 s, and the latter left mastoid process and 1 s).

The similarity in latencies between SEPs and SEFs was also observed in previous study (Mima et al., 1998). This result could be partly explained by the characteristics of MEG because MEG signals usually reflect the cortical activities that are derived from the intracellular current tangentially oriented to the scalp.

Kakigi and Shibasaki reported giant SEPs in response to tibial nerve stimulation in 3 patients with cortical reflex myoclonus due to various causes (progressive myoclonic epilepsy, sialidosis and uremic encephalopathy) (Kakigi and Shibasaki, 1987b). They showed enhanced P1–N1 components localized maximum at Cz or CPz. Their findings are consistent with our scalp SEPs in terms of amplitude. In their study, one patient showed delayed P1 and N1 components, as seen in our patient.

Paired SEPs demonstrated that the SEP2 was less suppressed, as compared with other ISIs, both at SI and MI for the ISIs of 40 and 200 ms. Decreased inhibition around ISI 40 ms was similar to the previous upper limb studies (Shibasaki et al., 1985; Ugawa et al., 1991). This consistent result between upper and lower limb giant SEPs indicates the mechanism of disinhibition at ISI of 40 ms which could be explained by the intracortical factors after the somatosensory afferent signals reach the SI. It could correlate with exaggerated scalp recorded 16–20 Hz (interval of 42–50 ms) oscillatory EEG potentials over the contralateral SMI in patients with positive or negative myoclonus (Ugawa et al., 2003). On the other hand, disinhibition at ISI of 200 ms could be explained by the earlier recovery usually almost completed at ISI of 300 ms in normal subjects (Ugawa et al., 1991). SEP2 was suppressed by the preceding stimulus (SEP1) to a lesser degree, as compared with other ISIs, but it was still less than 100% of the SEP1 at ISIs of 40 and 200 ms, as opposed to more than 100% of SEP1 in the previous studies (Shibasaki et al., 1985; Ugawa et al., 1991). It may be explained by the fact that the present patient was treated by many kinds of anticonvulsants that could enhance inhibitory activity within the brain. The effect of anticonvulsants and epileptic activity on the result of single pulse as well as paired pulse SEPs remains to be taken into consideration.

Acknowledgements

This study was supported by the Research Grant for the Treatment of Intractable Epilepsy (16-1) from the Japan Ministry of Health, Labor and Welfare, the Scientific Research Grant (C2) 18590935 from the Japan Society for the Promotion of Science (JSPS), Nakayama Foundation for Human Science, the Grants-in-Aid for Young Scientists (B) 17790578 from the Japan Ministry of Education, Culture, Sports, Science and Technology (MEXT), Kanae Foundation for life and socio-medical science.

References

Brown P, Day BL, Rothwell JC, Thompson PD, Marsden CD. Intrahemispheric and interhemispheric spread of cerebral cortical myoclonic activity and its relevance to epilepsy. Brain 1991;114:2333–51.

Cowan JM, Rothwell JC, Wise RJ, Marsden CD. Electrophysiological and positron emission studies in a patient with cortical myoclonus, epilepsia partialis continua and motor epilepsy. J Neurol Neurosurg Psychiatry 1986;49:796–807.

Hitomi T, Ikeda A, Matsumoto R, Kinoshita M, Taki J, Usui K, Mikuni N, Nagamine T, Hashimoto N, Shibasaki H. Subdural recording of giant somatosensory evoked potentials (SEPs): a comparison between primary motor (MI) and sensory cortex (SI) (abstract). Eighth international evoked potentials symposium; 2004. p. 416.

Ikeda A, Shibasaki H, Nagamine T, Xu X, Terada K, Mima T, Kaji R, Kawai I, Tatsuoka Y, Kimura J. Peri-rolandic and fronto-parietal components of scalp-recorded giant SEPs in cortical myoclonus. Electroencephalogr Clin Neurophysiol 1995;96:300–9.

Kakigi R, Shibasaki H. Generator mechanisms of giant somatosensory evoked potentials in cortical reflex myoclonus. Brain 1987a;110:1359–73.

Kakigi R, Shibasaki H. Somatosensory evoked potentials following stimulation of the lower limb in cortical reflex myoclonus. J Neurol Neurosurg Psychiatry 1987b;50:1641–6.

Matsumoto R, Kinoshita M, Taki J, Hitomi T, Mikuni N, Shibasaki H, Fukuyama H, Hashimoto N, Ikeda A. In vivo epileptogenicity of focal cortical dysplasia: a cortical paired stimulation study. Epilepsia 2005; 46:1744–9.

Mikuni N, Ikeda A, Yoneko H, Amano S, Hanakawa T, Fukuyama H, Hashimoto N. Surgical resection of an epileptogenic cortical dysplasia in the deep foot sensorimotor area. Epilepsy Behav 2005;7(3):559–62.

Mima T, Nagamine T, Nishitani N, Mikuni N, Ikeda A, Fukuyama H, Takigawa T, Kimura J, Shibasaki H. Cortical myoclonus: sensorimotor hyperexcitability. Neurology 1998;50:933–42.

Nakagawa Y, Matsumoto R, Ikeda A, Mikuni N, Matsuhashi M, Hanakawa T, Fukuyama H, Shimohama S. Focal cortical dysplasia at the primary somatosensory cortex could manifest both intractable partial epilepsy and cortical reflex myoclonus. Clin Neurol (Tokyo) (only abstract in English), in press.

Shibasaki H, Yamashita Y, Neshige R, Tobimatsu S, Fukui R. Pathogenesis of giant somatosensory evoked potentials in progressive myoclonic epilepsy. Brain 1985;108:225–40.

Shibasaki H, Nakamura M, Nishida S, Kakigi R, Ikeda A. Wave form decomposition of 'giant SEP' and its computer model for scalp topography. Electroencephalogr Clin Neurophysiol 1990;77:286–94.

Terao Y, Ugawa Y, Hanajima R, Yumoto M, Kawahara Y, Yamamoto T, Shirouzu I, Kanazawa I. Motor cortical reflex myoclonus: a case study with MEG. Electroencephalogr Clin Neurophysiol 1997;102:505–11.

Tyner FS, Knott JR, Mayer Jr WB. Fundamentals of EEG technology, vol. 1; 1983. p. 49–50.

Uesaka Y, Terao Y, Ugawa Y, Yumoto M, Hanajima R, Kanazawa I. Magnetoencephalographic analysis of cortical myoclonic jerks. Electroencephalogr Clin Neurophysiol 1996;99:141–8.

Ugawa Y, Genba K, Shimpo T, Mannen T. Somatosensory evoked potential recovery (SEP-R) in myoclonic patients. Electroencephalogr Clin Neurophysiol 1991;80:21–5.

Ugawa Y, Hanajima R, Terao Y, Kanazawa I. Exaggerated 16–720 Hz motor cortical oscillation in patients with positive or negative myoclonus. Clin Neurophysiol 2003;114:1278–84.

Acta Crystallographica Section F
Structural Biology and Crystallization Communications
ISSN 1744-3091

Structure of human ubiquitin-conjugating enzyme E2 G2 (UBE2G2/UBC7)

Ryoichi Arai,[a,b]‡ Seiko Yoshikawa,[a]‡ Kazutaka Murayama,[a,c] Yuzuru Imai,[d] Ryosuke Takahashi,[d,e] Mikako Shirouzu[a,b] and Shigeyuki Yokoyama[a,b,f]*

[a]Protein Research Group, RIKEN Genomic Sciences Center, Tsurumi, Yokohama 230-0045, Japan, [b]RIKEN SPring-8 Center, Harima Institute, Sayo, Hyogo 679-5148, Japan, [c]Tohoku University Biomedical Engineering Research Organization, Aoba, Sendai 980-8575, Japan, [d]RIKEN Brain Science Institute, Wako, Saitama 351-0198, Japan, [e]Department of Neurology, Graduate School of Medicine, Kyoto University, Sakyo, Kyoto 606-8507, Japan, and [f]Department of Biophysics and Biochemistry, Graduate School of Science, The University of Tokyo, Bunkyo, Tokyo 113-0033, Japan

‡ These authors contributed equally to this work.

Correspondence e-mail: yokoyama@biochem.s.u-tokyo.ac.jp

Received 22 December 2005
Accepted 10 March 2006

PDB Reference: human UBE2G2/UBC7, 2cyx, r2cyxsf.

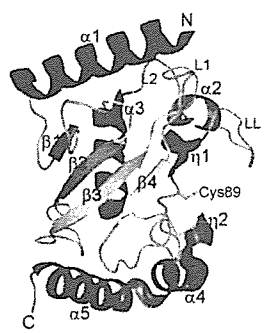

The human ubiquitin-conjugating enzyme E2 G2 (UBE2G2/UBC7) is involved in protein degradation, including a process known as endoplasmic reticulum-associated degradation (ERAD). The crystal structure of human UBE2G2/UBC7 was solved at 2.56 Å resolution. The UBE2G2 structure comprises a single domain consisting of an antiparallel β-sheet with four strands, five α-helices and two 3_{10}-helices. Structural comparison of human UBE2G2 with yeast Ubc7 indicated that the overall structures are similar except for the long loop region and the C-terminal helix. Superimposition of UBE2G2 on UbcH7 in a c-Cbl–UbcH7–ZAP70 ternary complex suggested that the two loop regions of UBE2G2 interact with the RING domain in a similar way to UbcH7. In addition, the extra loop region of UBE2G2 may interact with the RING domain or its neighbouring region and may be involved in the binding specificity and stability.

1. Introduction

Ubiquitin-dependent protein degradation plays an important role in the regulation of various cellular processes, including cell-cycle progression, signal transduction, transcription, DNA repair and protein quality control (Koepp *et al.*, 1999; Laney & Hochstrasser, 1999). Ubiquitination involves the successive actions of the ubiquitin-activating (E1), ubiquitin-conjugating (E2) and ubiquitin-protein ligase enzymes (E3) (Hershko & Ciechanover, 1998; Pickart, 2001). The E1 enzyme activates free ubiquitin and transfers it to E2 through a thioester linkage between the ubiquitin C-terminus and an E2 active-site cysteine. The E3 enzyme recognizes its substrate and E2 and catalyzes the formation of an isopeptide bond between a lysine ε-amino group of the substrate (or ubiquitin) and the C-terminal carboxyl group of ubiquitin Gly76. Over 30 human E2s have been identified and they all contain a conserved ~150 amino-acid catalytic core. The E2 enzymes are grouped into four classes depending on the presence and the location of additional sequences (Jentsch, 1992). Some of these enzymes contain extra C-terminal and/or N-terminal extensions from the core domain. The class I enzymes are the smallest E2 enzymes and consist almost entirely of the conserved core domain. The class II enzymes contain an extra C-terminal extension from the core domain, while class III enzymes have an N-terminal extension. The class IV enzymes contain both N- and C- terminal extensions.

The human UBE2G2 gene encodes the ubiquitin-conjugating enzyme E2 G2 (UBE2G2/UBC7), with a molecular weight of 18.6 kDa (165 amino acids). It was mapped to the region of human chromosome 21q22.3 and its transcripts are ubiquitously expressed in human tissues (Katsanis & Fisher, 1998; Rose *et al.*, 1998). Human UBE2G2 is a class I E2 enzyme. Recently, bacterial expression of His-tagged human UBE2G2 was reported (Reyes *et al.*, 2006). The human UBE2G2 protein shares 100, 62, 47 and 27% identities to murine UBE2G2/UBC7 (MmUBC7), yeast Ubc7, human UBE2G1 and human UbcH7, respectively (Fig. 1*a*). The crystal structures of yeast Ubc7 (Cook *et al.*, 1997), a human E6AP–UbcH7 complex (Huang *et*

al., 1999) and a human c-Cbl–UbcH7–ZAP-70 complex (Zheng *et al.*, 2000) have been reported. Functional studies have associated yeast Ubc7 and MmUBC7 with the degradation of endoplasmic reticulum (ER) substrates, a process known as ER-associated degradation (ERAD; Jungmann *et al.*, 1993; Fang *et al.*, 2001; Tiwari & Weissman, 2001). Parkin, a gene product responsible for autosomal recessive juvenile Parkinsonism (AR-JP), interacts with human UBE2G2/UBC7 and UBC6 through its RING domain and specifically ubiquitinates the Pael receptor in the presence of the E2s (Imai *et al.*, 2001). Furthermore, exogenous MmUBC7 mediates the ubiquitination and down regulation of both the inositol 1,4,5-triphosphate receptor in human neuroblastoma cells (Webster *et al.*, 2003) and the human type 2 iodothyronine selenodeiodinase (Kim *et al.*, 2003). Recently, the interactions of human UBE2G2/UBC7 with some RING-finger E3s, such as human HRD1 (Kikkert *et al.*, 2004) and TEB4 (Hassink *et al.*, 2005), have been reported. To analyze the structural and functional details of human UBE2G2/UBC7, which is involved in important cellular processes, its structure must be determined and compared with those of its homologues. Here, we report the crystal structure of human UBE2G2/UBC7 at 2.56 Å resolution and discuss its structural aspects.

2. Materials and methods

2.1. Protein expression and purification

The human UBE2G2 gene (Imai *et al.*, 2001) encoding human ubiquitin-conjugating enzyme E2 G2 (UBE2G2/UBC7) was cloned into a modified pENTR vector with a tobacco etch virus (TEV) protease cleavage site, derived from pENTR1A (Invitrogen). The expression vector pET/cMBP-UBE2G2 was constructed using Gateway technology (Invitrogen) with pENTR/TEV-UBE2G2 and pET/cMBP-GATEWAY bearing a T7 promoter, an N-terminal maltose-binding protein (MBP) tag and a Gateway reading frame cassette A (Invitrogen). The UBE2G2 protein was expressed as a fusion with an N-terminal MBP tag and a TEV protease cleavage site in *Escherichia coli* BL21(DE3). The protein was first purified on an amylose-resin column (New England Biolabs) and the MBP tag was then cleaved by His-tagged TEV protease, which was removed using a HisTrap column (GE Healthcare). The protein was purified further by Mono-Q and Superdex 75 column (GE Healthcare) chromatography steps. The yield of purified UBE2G2 protein was 8 mg per litre of culture. The construct that was used for crystallization contained the cloning artifact sequence GGSEF at the N-terminus.

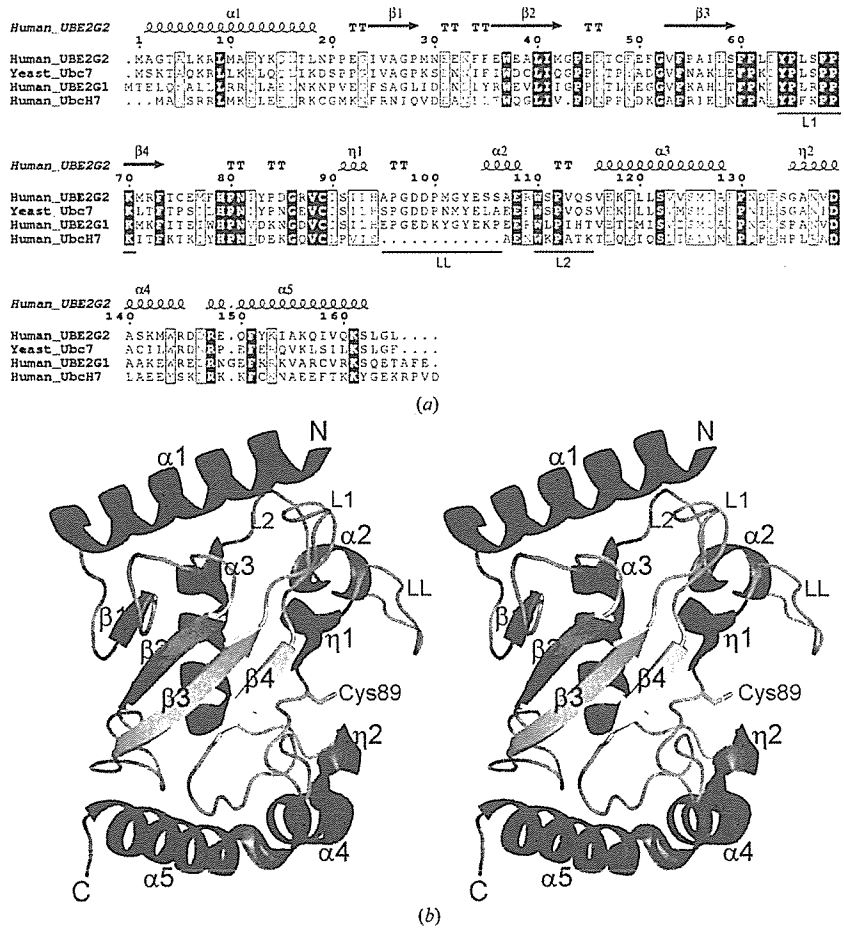

Figure 1
(*a*) Sequence alignment of homologues of human UBE2G2/UBC7. The alignment was generated by *ESPript* (Gouet *et al.*, 1999) with *CLUSTAL W* (Thompson *et al.*, 1994). The secondary structures of the human UBE2G2 protein, as determined by *DSSP* (Kabsch & Sander, 1983), are shown above the sequences (α, α-helix; β, β-strand; η, 3_{10}-helix; TT, β-turn). (*b*) Ribbon representation of the human UBE2G2/UBC7 structure (amino acids 1–165; stereoview). The helices and the β-strands are shown in red and yellow, respectively. The active-site residue (Cys89) is shown as a stick model.

2.2. Crystallization and data collection

Preliminary crystals of human UBE2G2 were obtained under condition No. 42 (0.1 *M* Tris–HCl buffer pH 8.5 containing 1.5 *M* ammonium sulfate and 12% glycerol) of the Crystal Screen 2 crystal screening kit (Hampton Research) using the 96-well sitting-drop vapour-diffusion method. The crystals of UBE2G2 used for structure determination were obtained in drops composed of 1 µl 8.5 mg ml^{-1} protein solution (20 m*M* Tris–HCl buffer pH 8.0 containing 120 m*M* NaCl, 2 m*M* DTT) and 1 µl reservoir solution (0.1 *M* Tris–HCl buffer pH 8.1 containing 1.45 *M* ammonium sulfate and 12% glycerol; Hampton Research) by the hanging-drop vapour-diffusion method against 500 µl reservoir solution. A rod-like crystal (~350 × 100 × 100 µm) was obtained within a few days and was used for data collection. The data collection was carried out at 100 K, with the reservoir solution containing 27.5% glycerol as a cryoprotectant. The diffraction data were collected at SPring-8 BL26B1 (Yamamoto *et al.*, 2002) and were recorded on a Jupiter 210 CCD detector (Rigaku). All diffraction data were processed with the *HKL*2000 program suite (Otwinowski & Minor, 1997).

2.3. Structure determination and refinement

The structure was solved by the molecular-replacement method using *MOLREP* (Vagin & Teplyakov, 1997) with the yeast Ubc7 structure (PDB code 2ucz; Cook *et al.*, 1997) as a search model. Data in the resolution range 50–3.0 Å were used in both rotation and translation calculations, which gave an obvious solution with significant contrast, resulting in three molecules in the asymmetric unit with a Matthews coefficient (V_M) of 3.83 $Å^3$ Da^{-1} and a solvent content of 67.91%. The model was corrected iteratively using *O* (Jones *et al.*, 1991) and was refined to 2.56 Å using *LAFIRE* (Yao *et al.*, 2006), *REFMAC*5 (Murshudov *et al.*, 1997) and *Crystallography & NMR System* (*CNS*; Brünger *et al.*, 1998). The crystallographic data and refinement statistics are presented in Table 1. Since there was additional electron density, four residues of the cloning artifact sequence at the N-terminus were also modelled. The final model includes 507 amino-acid residues of three UBE2G2 monomers and 23 water molecules in the asymmetric unit. In the loop regions (residues 100–106 and 131–133), the electron density corresponding to the side chains was ambiguous, which increased the *B* factor. In addition, relatively large areas of the molecular surface were exposed to the solvent in the crystal as the solvent content was high. These features resulted in the high average *B* factor. The quality of the model was inspected using *PROCHECK* (Laskowski *et al.*, 1993). The figures were created using *PyMOL* (DeLano, 2005).

Table 1
X-ray data-collection and refinement statistics.

Values in parentheses are for the outer shell (2.65–2.56 Å).

Data collection	
Space group	$P2_12_12_1$
Unit-cell parameters (Å)	a = 63.52, b = 87.61, c = 157.41
Wavelength (Å)	1.000
Resolution (Å)	50–2.56
Total reflections	117935
Unique reflections	28705
Redundancy	4.1 (3.7)
Completeness (%)	97.5 (84.6)
$I/\sigma(I)$	22.2 (4.2)
R_{sym}† (%)	5.5 (29.3)
Refinement	
Resolution (Å)	49.43–2.56
No. of reflections	28395
No. of protein atoms	3996
No. of water molecules	23
R_{work} (%)	22.8
R_{free}‡ (%)	26.2
R.m.s.d. bond lengths (Å)	0.009
R.m.s.d. bond angles (°)	1.6
Average *B* factor ($Å^2$)	75.7
Ramachandran plot	
Most favoured regions (%)	85.9
Additional allowed regions (%)	14.1
Generously allowed regions (%)	0.0
Disallowed regions (%)	0.0

† $R_{sym} = \sum|I_i - I_{avg}|/\sum I_i$, where I_i is the observed intensity and I_{avg} is the average intensity. ‡ R_{free} is calculated for 10% of randomly selected reflections excluded from refinement.

3. Results and discussion

The crystal structure of human UBE2G2 comprises a single domain consisting of an antiparallel β-sheet with four strands (β1–β4), five α-helices (α1–α5) and two 3_{10}-helices (η1 and η2; Fig. 1*b*). The ubiquitin-accepting residue Cys89 is located near η1. The overall folding of UBE2G2 corresponds to the typical fold of ubiquitin-conjugating enzymes. According to analytical ultracentrifugation, the

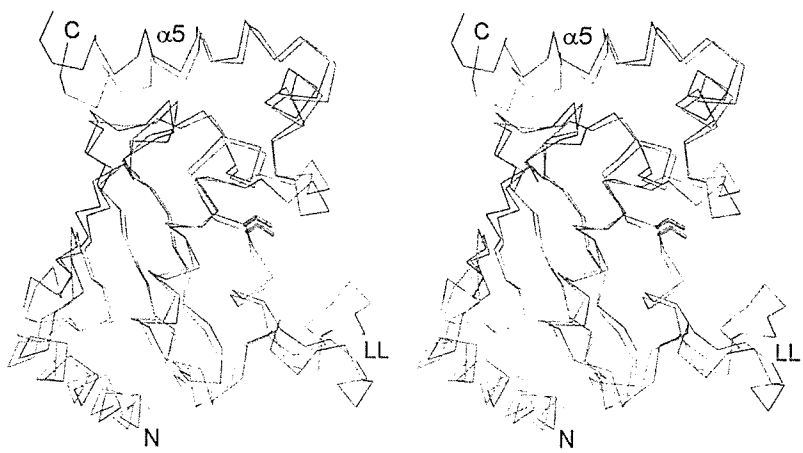

Figure 2
Superimposition of the main-chain structures of human UBE2G2 (green) and yeast Ubc7 (orange) (PDB code 2ucz; Cook *et al.*, 1997) (stereoview). The active-site cysteine residues are shown as stick models. The superimposition was carried out with *LSQKAB* (Kabsch, 1976).

molecular weight of UBE2G2 was ~18 kDa (data not shown), indicating that the UBE2G2 protein exists as a monomer in solution.

Fig. 2 shows the superimposition of the main-chain structures of human UBE2G2 and yeast Ubc7 (Cook *et al.*, 1997). The overall structure of UBE2G2 is remarkably similar to that of yeast Ubc7 (r.m.s.d. = 2.15 Å over 164 C^{α} atoms). The major differences between human UBE2G2 and yeast Ubc7 are the structure of the long loop (LL) region (95–106) and the angle of the C-terminal helix. The C-terminal helix (α5) of UBE2G2 is closer to the β-sheet core region than that of yeast Ubc7. The important interactions of UBE2G2 in the contact region of the C-terminal helix and the core region are the hydrophobic interactions among Phe54, Met77, Phe78, Ile154 and Ile158 and the salt bridge between Glu76 and Lys161. The residues Glu76, Ile154 and Ile158 are replaced with Ser76, Gln154 and Ser158 in yeast Ubc7, respectively, suggesting that the interactions of yeast Ubc7 are weaker than those of UBE2G2. Consequently, the angle of the C-terminal helix (α5) may change. Recently, the crystal structure of the human ubiquitin-conjugating enzyme E2 G1 (UBE2G1), which is another human homologue of yeast Ubc7, was deposited in the PDB (PDB code 2awf). A structural comparison of UBE2G2 with UBE2G1 revealed that the overall folding of UBE2G2 is similar to that of UBE2G1 (r.m.s.d. = 1.12 Å over 115 C^{α} atoms), but in UBE2G1 the residues 98–106 within the long loop (LL) region and the C-terminal helices (η2, α4 and α5) were not located in the model owing to disorder.

Zheng and coworkers reported the crystal structure of a c-Cbl–UbcH7–ZAP70 peptide ternary complex (PDB code 1fbv; Zheng *et al.*, 2000). It revealed how the RING domain of c-Cbl recruits the ubiquitin-conjugating enzyme UbcH7. Fig. 3(*a*) shows the superimposition of the main-chain structures of UBE2G2 and UbcH7 in the ternary complex. The overall folding of UBE2G2 and UbcH7 overlaps roughly (r.m.s.d. = 2.95 Å over 143 C^{α} atoms). Fig. 3(*b*) shows a close-up view of the interface between the RING domain and the E2s. The critical residues of UbcH7 for the interaction with the RING domain, Pro62, Phe63, Lys96, Pro97 and Ala98 (Zheng *et al.*, 2000), and the corresponding residues of UBE2G2, Pro65, Leu66,

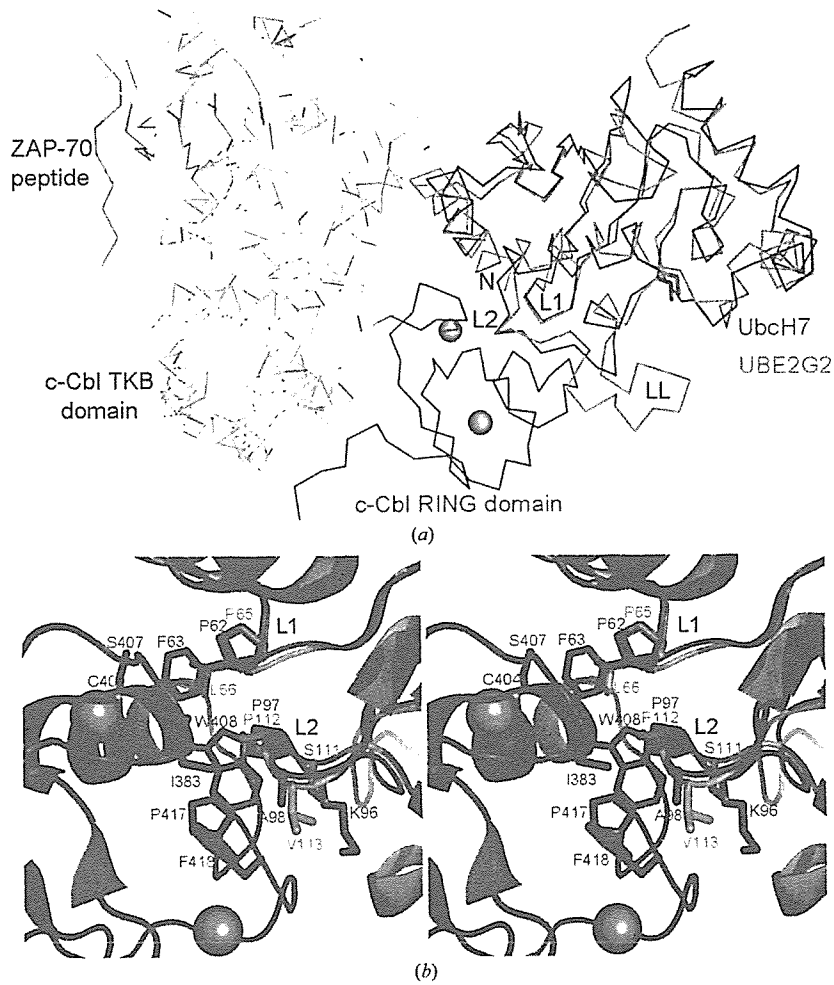

Figure 3
(*a*) Superimposition of the main-chain structures of human UBE2G2 and UbcH7 in the c-Cbl–UbcH7–ZAP70 peptide ternary complex (PDB code 1fbv; Zheng *et al.*, 2000). The TKB domain and linker sequence of c-Cbl, the RING domain of c-Cbl, the ZAP-70 peptide and human UbcH7 are coloured yellow, red, cyan and magenta, respectively. The zinc ions are indicated by grey spheres. The human UBE2G2 protein is coloured green. The active-site cysteine residues are shown as stick models. (*b*) Close-up view of the ribbon representation of the interface between the RING domain and UbcH7 in the c-Cbl–UbcH7–ZAP70 complex and the superimposition of UBE2G2 on UbcH7 (stereoview). The colouring is the same as that in Fig. 3(*a*). The critical residues for the interaction of UbcH7 with the *RING* domain and the corresponding residues of UBE2G2 are shown as stick models. All superimpositions were carried out with *LSQKAB* (Kabsch, 1976).

Ser111, Pro112 and Val113, overlap remarkably well (r.m.s.d. = 0.768 Å over five C^{α} atoms), suggesting that the L1 (64–70) and L2 (110–115) loops of UBE2G2 are involved in the interaction with the RING domain in a similar way as UbcH7. This is consistent with the previous results that Parkin binds to UBE2G2 as well as UbcH7 and ubiquitinates substrates (Imai *et al.*, 2000, 2001). In addition, UBE2G2 has the extra long loop (LL) region (95–106), which is probably located on the side near the RING domain. The *B* factor of the LL region is relatively high, implying the possibility of conformational flexibility. The LL region may interact with the RING domain or its neighbouring region and may be involved in the binding specificity and stability.

We thank Mr R. Akasaka and Dr M. Kukimoto-Niino for the analytical ultracentrifugation, Mr S. Kamo for computer maintenance and Ms A. Ishii, Ms K. Yajima, Ms M. Sunada and Ms T. Nakayama for clerical assistance. We also thank Dr M. Yamamoto for data collection at the RIKEN Structural Genomics beamline BL26B1 at SPring-8. This work was supported by the RIKEN Structural Genomics/Proteomics Initiative (RSGI), the National Project on Protein Structural and Functional Analyses, the Ministry of Education, Culture, Sports, Science and Technology of Japan.

References

Brünger, A. T., Adams, P. D., Clore, G. M., DeLano, W. L., Gros, P., Grosse-Kunstleve, R. W., Jiang, J.-S., Kuszewski, J., Nilges, M., Pannu, N. S., Read, R. J., Rice, L. M., Simonson, T. & Warren, G. L. (1998). *Acta Cryst.* D**54**, 905–921.

Cook, W. J., Martin, P. D., Edwards, B. F., Yamazaki, R. K. & Chau, V. (1997). *Biochemistry*, **36**, 1621–1627.

DeLano, W. L. (2005). *PyMOL* v.0.98. DeLano Scientific, South San Francisco, CA, USA.

Fang, S., Ferrone, M., Yang, C., Jensen, J. P., Tiwari, S. & Weissman, A. M. (2001). *Proc. Natl Acad. Sci. USA*, **98**, 14422–14427.

Gouet, P., Courcelle, E., Stuart, D. I. & Metoz, F. (1999). *Bioinformatics*, **15**, 305–308.

Hassink, G., Kikkert, M., van Voorden, S., Lee, S. J., Spaapen, R., van Laar, T., Coleman, C. S., Bartee, E., Fruh, K., Chau, V. & Wiertz, E. (2005). *Biochem. J.* **388**, 647–655.

Hershko, A. & Ciechanover, A. (1998). *Annu. Rev. Biochem.* **67**, 425–479.

Huang, L., Kinnucan, E., Wang, G., Beaudenon, S., Howley, P. M., Huibregtse, J. M. & Pavletich, N. P. (1999). *Science*, **286**, 1321–1326.

Imai, Y., Soda, M., Inoue, H., Hattori, N., Mizuno, Y. & Takahashi, R. (2001). *Cell*, **105**, 891–902.

Imai, Y., Soda, M. & Takahashi, R. (2000). *J. Biol. Chem.* **275**, 35661–35664.

Jentsch, S. (1992). *Annu. Rev. Genet.* **26**, 179–207.

Jones, T. A., Zou, J. Y., Cowan, S. W. & Kjeldgaard, M. (1991). *Acta Cryst.* A**47**, 110–119.

Jungmann, J., Reins, H. A., Schobert, C. & Jentsch, S. (1993). *Nature (London)*, **361**, 369–371.

Kabsch, W. (1976). *Acta Cryst.* A**32**, 922–923.

Kabsch, W. & Sander, C. (1983). *Biopolymers*, **22**, 2577–2637.

Katsanis, N. & Fisher, E. M. (1998). *Genomics*, **51**, 128–131.

Kikkert, M., Doolman, R., Dai, M., Avner, R., Hassink, G., van Voorden, S., Thanedar, S., Roitelman, J., Chau, V. & Wiertz, E. (2004). *J. Biol. Chem.* **279**, 3525–3534.

Kim, B. W., Zavacki, A. M., Curcio-Morelli, C., Dentice, M., Harney, J. W., Larsen, P. R. & Bianco, A. C. (2003). *Mol. Endocrinol.* **17**, 2603–2612.

Koepp, D. M., Harper, J. W. & Elledge, S. J. (1999). *Cell*, **97**, 431–434.

Laney, J. D. & Hochstrasser, M. (1999). *Cell*, **97**, 427–430.

Laskowski, R. A., MacArthur, M. W., Moss, D. S. & Thornton, J. M. (1993). *J. Appl. Cryst.* **26**, 283–291.

Murshudov, G. N., Vagin, A. A. & Dodson, E. J. (1997). *Acta Cryst.* D**53**, 240–255.

Otwinowski, Z. & Minor, W. (1997). *Methods Enzymol.* **276**, 307–326.

Pickart, C. M. (2001). *Annu. Rev. Biochem.* **70**, 503–533.

Reyes, L. F., Sommer, C. A., Beltramini, L. M. & Henrique-Silva, F. (2006). *Protein Expr. Purif.* **45**, 324–328.

Rose, S. A., Leek, J. P., Moynihan, T. P., Ardley, H. C., Markham, A. F. & Robinson, P. A. (1998). *Cytogenet. Cell Genet.* **83**, 98–99.

Thompson, J. D., Higgins, D. G. & Gibson, T. J. (1994). *Nucleic Acids Res.* **22**, 4673–4680.

Tiwari, S. & Weissman, A. M. (2001). *J. Biol. Chem.* **276**, 16193–16200.

Vagin, A. & Teplyakov, A. (1997). *J. Appl. Cryst.* **30**, 1022–1025.

Webster, J. M., Tiwari, S., Weissman, A. M. & Wojcikiewicz, R. J. (2003). *J. Biol. Chem.* **278**, 38238–38246.

Yamamoto, M., Kumasaka, T., Ueno, G., Ida, K., Kanda, H., Miyano, M. & Ishikawa, T. (2002). *Acta Cryst.* A**58**, C302.

Yao, M., Zhou, Y. & Tanaka, I. (2006). *Acta Cryst.* D**62**, 189–196.

Zheng, N., Wang, P., Jeffrey, P. D. & Pavletich, N. P. (2000). *Cell*, **102**, 533–539.